Article:
Meek, U, Piazolo, S and Daczko, NR (2019) The field and microstructural signatures of deformation-assisted melt transfer: Insights from magmatic arc lower crust, New Zealand. Journal of Metamorphic Geology, 37 (6). pp. 795-821. ISSN: 0263-4929

https://doi.org/10.1111/jmg.12488

Journal of METAMORPHIC GEOLOGY

The field and microstructural signatures of deformation-assisted melt transfer: Insights from magmatic arc lower crust of New Zealand

Journal:	*Journal of Metamorphic Geology*
Manuscript ID	JMG-18-0049.R2
Manuscript Type:	Original Article
Date Submitted by the Author:	n/a
Complete List of Authors:	Meek, Uvana; Macquarie University, Department of Earth and Planetary Sciences Piazolo, Sandra; Macquarie University, Department of Earth and Planetary Sciences; University of Leeds, School of Earth and Environment Daczko, Nathan; Macquarie University, Department of Earth and Planetary Sciences
Keywords:	reactive melt flow, dissolution-precipitation, melt-rock interaction, hornblendite

THE FIELD AND MICROSTRUCTURAL SIGNATURES OF DEFORMATION-ASSISTED MELT TRANSFER: INSIGHTS FROM MAGMATIC ARC LOWER CRUST, NEW ZEALAND

U. Meek, S. Piazolo, N. R. Daczko

Australian Research Council Centre of Excellence for Core to Crust Fluid Systems (CCFS) and GEMOC, Department of Earth and Planetary Sciences, Macquarie University, Sydney, NSW 2109, Australia

Short title: Channelized reactive melt flow in lower crust

ABSTRACT

Melt must transfer through the lower crust, yet the field signatures and mechanisms involved in such transfer zones (excluding dykes) are still poorly understood. We report field and microstructural evidence of a deformation-assisted melt transfer zone that developed in the lower crustal magmatic arc environment of Fiordland, New Zealand. A 30–40m wide hornblende-rich body comprising hornblende ± clinozoisite and/or garnet exhibits 'igneous-like' features and is hosted within a metamorphic, two-pyroxene-pargasite gabbroic gneiss. Previous studies have interpreted the hornblende-rich body as an igneous cumulate or a mass transfer zone. We present field and microstructural characteristics supporting the later and indicating the body has formed by deformation-assisted, channelized, reactive porous melt flow. The host granulite facies gabbroic gneiss contains distinctive rectilinear dykes and garnet reaction zones (GRZ) from earlier in the geological history; these form important reaction and strain markers. Field observations show that the mineral assemblages and microstructures of the gabbroic gneiss and GRZ are progressively modified with proximity to the hornblende-rich body. At the same time GRZ bend systematically into the hornblende-rich body on each side of the unit, showing apparent sinistral shearing. Within the hornblende-rich body itself, microstructures and EBSD mapping show evidence of the former presence of melt including observations consistent with melt crystallisation within pore spaces, elongate pseudomorphs of melt films along grain boundaries, minerals with low dihedral angles <10–<60º, and interconnected 3D melt pseudomorph networks. Reaction microstructures with highly irregular contact boundaries are observed at the field and thin-section scale in remnant islands of original rock and replaced grains, respectively. We infer that the hornblende-rich body was formed by modification of the host gabbroic gneiss in-situ due to reaction between an externally-derived, reactive, hydrous gabbroic to intermediate melt percolating via porous melt flow through an actively deforming zone. Extensive melt-rock interaction and metasomatism occurred via

coupled dissolution-precipitation, triggered by chemical disequilibrium between the host rock and the fluxing melt. As a result, the host plagioclase and pyroxene became unstable and were reacted and dissolved into the melt, while hornblende and to a lesser extent clinozoisite and garnet grew replacing the unstable phases. Our study shows that hornblendite rocks commonly observed within deep crustal sections, and attributed to cumulate fractionation processes, may instead delineate areas of deformation-assisted, channelized reactive porous melt flow formed by melt-mediated coupled dissolution-precipitation replacement reactions.

Keywords: reactive melt flow, dissolution-precipitation, melt-rock interaction, hornblendite

INTRODUCTION

It is well established that heat transfer from the Earth's mantle to the surface is crucial for continental differentiation and driving plate tectonics, and thus must involve significant mass transfer (via migration of melt) through the crust (Bercovici, 2003; Brown, 2010; Gurnis, 1988; Schubert, Turcotte, & Olson, 2001). Our understanding of the mechanisms of melt transfer in crustal zones is limited to channelled melt transfer through dykes and melt-bearing shear zones, yet the number and volume of these pathways are too small to accommodate the heat and mass transfer necessary for chemical differentiation (Rudnick, 1995). Pervasive melt movement (Brown, 2010; Hasalová, Schulmann, et al., 2008a; Sawyer, 1999; Weinberg, 1999) is not well understood, but may explain the discrepancy between recognized former melt pathways and necessary melt transfer needed within our Earth system. This discrepancy focusses attention on an existing gap in our ability to identify former melt pathways in the geological record.

To identify these cryptic melt pathways, indicative field relationships and microstructures need to be established. While the signatures related to melt flux through dykes (Sleep, 1988; Spence, Sharp, & Turcotte, 1987; Weinberg, 1996) or melt-bearing shear zones (Beach & Fyfe, 1972; Carter & Dworkin, 1990; Cartwright & Barnicoat, 2003; Lee, Torvela, Lloyd, & Walker, 2018; Streit & Cox, 1998; Stuart, Piazolo, & Daczko, 2018) have been well-documented in the continental crust, those associated with the third possible pervasive movement mechanism of porous melt flow, are largely lacking. The latter process involves melt flow along grain boundaries and within grain triple junctions, where the melt forms a highly connected network (Scott & Stevenson, 1986; Turcotte & Ahern, 1978). This contrasts to easily recognised field relationships where melt segregated to form a dyke or in the case of shear zones that preserve a high proportion of crystallised melt (Vanderhaeghe, 1999; Weinberg & Searle, 1998). Porous melt flow can be buoyancy-driven (Solano, Jackson, Sparks, Blundy, & Annen, 2012) or stress-driven via deformation (Hasalová, Schulmann, et al., 2008a).

There are several styles of porous melt flow where intragranular melt movement is diffusive (passive movement along grain boundaries), channelized (restricted within channels, commonly physically or chemically armoured), and/or reactive (reactions at grain boundaries between melt and mineral) (Stuart, Meek, Daczko, Piazolo, & Huang, 2018).

Porous melt flow styles have been largely invoked for melt movement in the mantle, where the associated chemical and mineralogical changes are well documented (Dijkstra, Barth, Drury, Mason, & Vissers, 2003; Kelemen, Dick, & Quick, 1992; Kelemen, Shimizu, & Salters, 1995; Rampone, Piccardo, Vannucci, Bottazzi, & Zanetti, 1994). In particular, formation of dunite channels (Aharonov, Whitehead, Kelemen, & Spiegelman, 1995; Braun & Kelemen, 2002; Kelemen et al., 1995; Spiegelman, Kelemen, & Aharonov, 2001) and harzburgite channels (Kelemen et al., 1992) in the mantle have been attributed to formation via porous melt flow, and subsequent metasomatism. The increased interest in porous melt flow processes in the mantle occurred where classic mantle geochemical signatures were not found, for example where geochemical compositions of mafic rocks were too enriched or depleted in major, trace or rare earth elements to be derived from primitive mantle. In many cases, melt-rock interactions induced metasomatism of the mantle via coupled dissolution-precipitation replacement reactions, all facilitated by porous melt flow.

More recently, porous melt flow has also been suggested for melt movement in the Earth's oceanic crust (Collier & Kelemen, 2010; Coogan, Saunders, Kempton, & Norry, 2000; Lissenberg, MacLeod, Howard, & Godard, 2013; Lissenberg & Dick, 2008; Rampone et al., 2016; Sanfilippo et al., 2015) and arc crust (Cashman, Sparks, & Blundy, 2017; Daczko, Piazolo, Meek, Stuart, & Elliott, 2016; Smith, 2014; Stuart, Daczko, & Piazolo, 2017; Stuart, Meek, et al., 2018; Stuart, Piazolo, & Daczko, 2016; Wu et al., 2018; Závada et al., 2018). Many of these studies have focussed primarily on the geochemical signatures found in lower arc and oceanic crustal sequences, which could not be explained by typical crystal fractionation

from primitive magmas. Due to the relatively low viscosity contrasts of melt and rock within the lower arc crust, porous melt flow within the crust is believed to require deformation to proceed efficiently (Hasalová, Schulmann, et al., 2008a). However, porous melt flow has been shown to occur in both static and dynamic environments (Stuart et al., 2017; Stuart, Meek, et al., 2018; Stuart et al., 2016).

The aim of this contribution is to develop an in-depth understanding of the mechanisms involved in deformation-assisted, channelized reactive porous melt flow in lower arc crust and therefore identify its expression from the field to the micron scale. We examine a hornblende-rich body (i.e. hornblendite), commonly found in mafic crust (e.g. Daczko, Emami, Allibone, & Turnbull, 2012; Debari, Kay, & Kay, 1987; Fanka et al., 2016; Pál-Molnár et al., 2015) typically characterised as igneous cumulates. We show in this study, a hornblendite which exhibits features that preclude an igneous cumulate origin and instead presents evidence for formation via reactive porous melt flow through lower crustal gabbroic gneiss, accommodated by shear zone deformation and chemical armouring, that results in grain-scale coupled dissolution-precipitation replacement reactions. Within this contribution, we refer to the host rock as gabbroic gneiss, and the hornblende-rich body or hornblendite as the reaction product. Our results suggest that porous melt flow may play a larger role within lower arc crustal environments as well as early earth crustal formation (Sizova, Gerya, Stüwe, & Brown, 2015) and invites further work in identifying cryptic mass transfer zones and their expression.

REGIONAL GEOLOGY AND PREVIOUS WORK

We chose the field area due to its exceptional exposure, absence of post-melt flux overprint and frequency of such melt transfer zones from the cm to 10s m scale (e.g. Daczko et al. 2016, Stuart et al. 2018). The field area lies in the Pembroke Valley located in New Zealand's South Island (Fig. 1a) and represents one of the few exposed lower crustal sections of magmatic arc

117 crust that preserves nearly exclusively deep arc conditions (Allibone et al., 2009; Blattner,
118 1991; Chapman, Clarke, & Daczko, 2016; Chapman, Clarke, Piazolo, & Daczko, 2017; Clarke,
119 Fitzherbert, Milan, Daczko, & Degeling, 2010; Clarke, Klepeis, & Daczko, 2000; De Paoli,
120 Clarke, & Daczko, 2012; Milan, Daczko, & Clarke, 2017; Milan, Daczko, Clarke, & Allibone,
121 2016; Mortimer et al., 1999). Within the Pembroke Valley, the so-called Pembroke Granulite
122 is exposed. This granulite is part of the Median Batholith, comprising Carboniferous to Early
123 Cretaceous magmatic arc rocks which were rapidly exhumed with little to no
124 tectonometamorphic overprint (Blattner, 1976; Bradshaw, 1990; Clarke et al., 2000; Daczko,
125 Clarke, & Klepeis, 2001a; Daczko, Klepeis, & Clarke, 2001b).

126 The Pembroke Granulite is a low-strain gabbroic gneiss (GG) with pervasive foliation,
127 exhibiting a two-pyroxene-pargasite-plagioclase assemblage. Its igneous protolith was
128 emplaced at 139–129 Ma (Hollis, Clarke, Klepeis, Daczko, & Ireland, 2003) or 163–150 Ma,
129 (Stowell, Tulloch, Zuluaga, & Koenig, 2010).

130 The gabbroic igneous assemblage (enstatite, diopside, pargasite, plagioclase, ilmenite) was
131 variably recrystallised during D_1, forming a strongly aligned, steeply dipping S_1 gneissosity
132 striking NE. The granulite facies gneissosity is defined by alignment of pargasite and preferred
133 orientation of recrystallized clusters of enstatite, diopside and plagioclase (Clarke et al., 2000).
134 Similar syn-deformational metamorphic assemblages in nearby orthogneiss bodies formed at
135 lower crustal conditions of 850ºC and <11 kbar (Daczko & Halpin, 2009). A recent study
136 showed that the S_1 assemblage records a post-tectonic partial hydration during an early episode
137 of incipient melt-assisted diffuse porous melt flow (Stuart, Meek, et al., 2018). During melt-
138 rock interaction with an externally-derived, hydrous melt, the S_1 assemblage became partially
139 hydrated post-D_1, to pargasite, quartz, clinozoisite and plagioclase at 630–710ºC and 8.8–12.4
140 kbar (Stuart et al., 2017; Stuart et al., 2016).

A second tectonometamorphic event (D_2) is characterized by brittle fracturing associated with sub-vertical felsic dykes cutting the S_1 gneissosity. Two orthogonal rectilinear dyke orientations dominate (Daczko, Clarke, et al., 2001a). Within a halo of 1-10 cm associated with the crosscutting dykes, melt-rock dehydration reactions partially replace the S_1 and early porous melt flow assemblages, and transformed it nearly isochemically into garnet granulite (Blattner, 1976; Bradshaw, 1989a; Daczko, Clarke, et al., 2001a; Smith, Piazolo, Daczko, & Evans, 2015). Termed garnet reaction zones (GRZ) in previous literature, the melt-rock reactions occur as a result of volatile scavenging by the anhydrous trondhjemitic melt during melt flux through the dykes (Clarke et al., 2005). Melt-rock interaction conditions occurred at 720–890ºC and 12–16 kbar (Daczko & Halpin, 2009). D_3 deforms both D_1 and D_2 fabrics at granulite facies (676 ± 34ºC and 14 ± 1.26 kbar) forming narrow (cm–m) variably dipping shear zones (Daczko, Klepeis, et al., 2001b).

Besides the Pembroke Granulite of gabbroic composition, granulite with dioritic and ultramafic compositions have been reported, and the observed compositional range was attributed to variations in igneous protolith (Clarke et al., 2000; Daczko, Clarke, et al., 2001). However, recently the occurrence of these dioritic and ultramafic bodies have been reinterpreted to be indicative for moderate to extensive melt-rock interactions between gabbroic gneiss protoliths and externally-derived reactive melts (Daczko et al., 2016; Stuart, Meek, et al., 2018). The lenses of ultramafic composition, termed hornblende-rich bodies in this study, cut D_1-D_2, and is considered to be associated with either D_3 deformation or forms as the last deformational event (D_4) within the Pembroke Granulite geological history prior to rapid uplift.

The geochemical signatures of the hornblende-rich body are discussed in another contribution and there is referred to as Style 4 (Stuart, Meek, et al. (2018). Whole rock REE patterns of the hornblende-rich body show a middle-REE hump typical of hornblende cumulates. Amphibole in the hornblende-rich body is predominantly pargasite, with REE distributions increasing from

La to Eu (0.04-2.6 times chrondrite, a positive Eu anomaly, then flat yet enriched (up to 6 times chrondrite) MREE and HREE patterns. Clinozoisite (pistacite content between 12 and 18) is found across all four porous melt flow styles within the Pembroke Granulite (Stuart et al., 2018) with little appreciable changes in composition. REE patterns are typical of igneous clinozoisite, where LREE are significantly enriched, followed by a flat and steep HREE trend (Stuart et al., 2018).

METHODS

Petrographic analysis was completed using a petrographic microscope in combination with the Virtual Petrographic Microscope (Tetley & Daczko, 2014) on polished thin (30 μm) sections made from blocks cut from representative samples. Mineral identification and microstructural relationships of the samples were determined using plane-polarised light microscopy and back-scatter electron (BSE) imaging. BSE imaging was performed on a Hitachi Desktop Scanning Electron microscope (SEM; OptoFab node of the Australian National Fabrication Facility, Macquarie University) run at low vacuum, 15 kV accelerating voltage and working distances between 9–11 mm. Higher resolution imaging (15–30 kV, 10 nA beam current and working distances between 10–12.5 mm) was completed using a Carl Zeiss IVO scanning electron microscope (Macquarie University Geoanalytical (MQGA)).

Electron back-scatter diffraction (EBSD) analysis was performed on selected samples using the Carl Zeiss IVO SEM (MQGA) at 20kV and 8.0 nA. Patterns were acquired with HKL NordlysNano high sensitivity EBSD detector and indexed using AzTec analysis software (Oxford Instruments). Samples were tilted at 70º and analysed at working distances between 11–24.5 mm. Step sizes ranged between 1–8 μm dependent on the spatial resolution required. Channel 5 software was used for post-processing and all maps were cleaned using a "standard" noise reduction following Prior, Wheeler, Peruzzo, Spiess, and Storey (2002), Bestmann and

Prior (2003) and Piazolo, Bestmann, Prior, and Spiers (2006). Grain boundaries and subgrain boundaries have misorientations larger than 2° and less than 10º, respectively. Pole figures are equal area projections. EBSD mapping and analysis is applied to all samples used in the study, for consistency throughout the project.

Whole rock major element compositions were determined by XRF at the Mark Wainwright Analytical Centre, University of New South Wales (UNSW), Australia. Samples were processed using a PW2400 WDXRF Spectrometer. Whole rock powders were crushed using a hydraulic press with tungsten carbide plates and then reduced to a fine powder in a tungsten carbide barrel and ring Tema mill. Powders were fused into glass discs using lithium borate at 1050ºC for major element analysis. Loss on ignition (LOI) was established by heating the samples to 1050ºC for 1 hour.

FIELD RELATIONSHIPS

We report results from several occurrences of hornblende-rich rocks that cut the two-pyroxene-pargasite components of the Pembroke Granulite (Figure 1a inset). Samples are taken from two main sites. Site 1 exhibits a 30–40 m wide hornblende-rich body extending for >250 m along strike across the Pembroke Valley (Figure 1a). The outcrop was mapped in detail (Fig. 1b) and shows that the body consists of an irregularly shaped hornblende-rich rock body, surrounded by a 2–7 m wide zone characterized by hydration of the otherwise largely anhydrous host gabbroic gneiss. In the following, the latter zone is termed the transition zone. Samples were extracted in-situ from the main hornblende-rich body of this study (site 1), and are supplemented with samples from a smaller, 0.5–20 cm thick, continuous band of hornblendite that occurs over a distance of more than 100 m (site 2, Fig. 1c, d).

Characteristics of the host two-pyroxene-pargasite gabbroic gneiss (GG)

In outcrop, the host rock type is a two-pyroxene-pargasite gneiss (Pembroke Granulite). It has a pervasive S_1 gneissosity defined by preferred orientation of coarse-grained and partially recrystallized igneous pyroxenes (enstatite, diopside), pargasitic hornblende and plagioclase (Fig. 2a, 2a inset, 2b, 2c, Table 1). Recrystallization is most pronounced in plagioclase. A common feature of the Pembroke Granulite is the occurrence of wide-spread rectilinear dyking (Fig. 2a). This dyking pattern is easily discernible in the field as dykes are always associated with 2–5 cm wide garnet reaction zones (GRZ) either side of the dykes (Fig. 2a, Table 1). The S_1 gneissic foliation is often partially preserved both in the gabbroic gneiss (Fig. 2b) and GRZ (Fig. 2c) (Fig. 2a-c).

Characteristics of the hornblende-rich bodies (H)

The hornblende-rich bodies strike at an angle to the gneissosity of the gabbroic gneiss and GRZ. The hornblende-rich bodies are typically composed of >50–90% hornblende (pargasitic) with minor minerals (clinozoisite, garnet and plagioclase). Three main rock types of the hornblende-rich bodies are distinguished: (i) clinozoisite-hornblendite (H(Cz-Hbl)) (>10 area % clinozoisite), (ii) hornblendite sensu stricto (H(Hbl)) (<10 area % clinozoisite) and (iii) pegmatite (P) (Fig. 1b). In addition, throughout the hornblende-rich body, cm-wide bands of garnetite (± rare plagioclase and hornblende) are present within all rock types (Table 1).

Clinozoisite-hornblendite (H(Cz-Hbl)) is the dominant rock type, yet in places is cut by anastomosing zones of hornblendite (Fig. 1b., 3a). Hornblende is dark-coloured and coarse-grained (up to 5mm width) in both clinozoisite-hornblendite and hornblendite (Fig. 3a). Clinozoisite grains are pale green and elongate (up to 5mm length) with aspect ratios of 2–5. They are found randomly oriented (Fig. 3a), except close the hornblendite body–transition zone boundary where they are mapped to delineate high-strain zones based on their shape preferred

orientation subparallel to the boundaries of the hornblendite body (Fig. 1b). Plagioclase (< 5 area %) occurs as an interstitial mineral in both rock types (Fig. 3a).

Pegmatite bodies are found throughout the Site 1 hornblendite; these vary in size from small pegmatitic domains (cm-scale) to extensive pegmatite bodies (m-scale) (Fig. 1b, 3b, 3b inset). Pegmatite consists of elongate, euhedral crystals of hornblende (up to 10 cm length), tabular plagioclase (up to 10 cm length) and euhedral garnet (1–10 cm) (Fig. 3b, 3b inset). Pegmatite is hosted within both clinozoisite-hornblendite and hornblendite. Pegmatite bodies are generally irregularly shaped on all scales (cm-m scale) (Fig. 3b) and may completely embody and surround areas of the hornblende-rich body (Fig. 3b, 3b inset).

Garnet is the main constituent of distinct bands of garnetite, named garnetite stringers (Fig. 3c). The garnetite stringers are thin (<2–5cm wide), medium to coarse grained, and dominated by ~90–95 area % garnet, with minor fine-grained plagioclase and hornblende (Fig. 3c, Table 1). Garnetite stringers are continuous over several meters to tens of meters, found within both clinozoisite-hornblendite and hornblendite (Fig. 3a, c, d, Fig. 4f) and as fragments in the pegmatitic bodies (Fig. 3b).

In some areas, single, isolated euhedral (1–10 cm) garnet grains are seen in the hornblende-rich body (Fig. 3c, Table 1). These garnets are dark red in colour, notably inclusion free and may be surrounded by a thin 1–5 mm rim of plagioclase aggregates (Fig. 3d, 3d inset). These isolated garnets may also occur within or in close proximity to pegmatite bodies (Fig. 3b) and are found frequently close to the boundary of these rock units to the transition zone (Fig. 3d).

Characteristics of the transition zone (TZ)

The transition zone forms an irregular halo either side of the hornblende-rich body, ranging between 2–7 m in width for Site 1 (Fig. 1b) and more than 5 m for Site 2. This zone is defined as a portion of host two-pyroxene-pargasite gneiss (i.e. Pembroke Granulite), where the mineral

assemblages of both the gneiss and GRZ (sensu stricto) have been hydrated. The transition zone is formed by a hornblende-feldspar gneiss where, instead of pyroxene clusters, elongate clusters of hornblende pseudomorph the variably transposed S_1 gneissosity (Fig. 2a, 10a, Table 1). The prevalent GRZ markers from the two pyroxene-pargasite gneiss are found to be progressively mineralogically modified (Fig. 4a, Fig. 5c, d). The typical 5 cm wide GRZ (sensu stricto) becomes thinner, reduced to ~1–2 cm widths (Fig. 4a, 5a, b), and is surrounded by either feldspar or hornblende (Fig. 4a, Fig. 5c,d). Individual GRZ from the host rock (two-pyroxene-pargasite gneiss) can be traced continuously through the transition zone and directly into the hornblende-rich body (Fig. 5a, b) where they become the garnetite stringers, discussed above (Fig. 3a–d). Furthermore, the S_1 gneissic foliation present in the host rock can be traced into the foliated transition zone. However, the two-pyroxene assemblage has been hydrated to pargasite (Table 1).

There are several distinct, angular to rounded “islands” of transition zone within the hornblende-rich body ranging in scale from 30 cm–8 m length (Fig. 1b, 3e, f). They are generally lozenge-shaped, low-strain bodies exhibiting as the rest of the transition zone with a distinct pargasite defined gneissic foliation, inferred to be a transposed, pseudomorphed and hydrated S1 fabric (Fig. 3e, f).

Contact Relationships

The boundaries between the transition zone and hornblende-rich body are irregular, but sharp, and easily discernible due to the pronounced colour change and complete loss of the gneissic foliation seen within the transition zone but not in the hornblende-rich body (Fig. 4b, c, Table 1). The boundary is characterized by finger-like protrusions of hornblende-rich body into the transition zone which gradually thin to a sharp point (Fig. 4b, c, d, Fig. 5a). These sharp points are spatially associated with the mineralogically modified GRZ in the transition zone (Fig. 5a).

These modified GRZ are continuous to garnetite stringers in the hornblende-rich body. While the highly irregular boundary is a common feature, some contact boundaries are regular and lack hornblende-rich body protrusions (Fig. 1b, Fig. 4d, Fig. 5b). In these cases, GRZ are sub-parallel to parallel to the boundary between transition zone and the hornblende-rich body (Fig. 5a, b).

The boundary between the host gneiss and transition zone is less well-defined in the field. It is characterized by two main features; a distinct change in mineralogy of the GRZ and loss of pyroxene (as described above) resulting in hornblende being the main mafic mineral. Different to the boundary between hornblende-rich body and the transition zone, the gneissic S_1 foliation is continuous across the boundary (Fig. 4c, d).

Strain variations

The fact that GRZ have a well-defined rectilinear pattern within the host rock and can be continuously traced into the transition zone and hornblende-rich body, allows their use as reaction and strain markers utilizing the orientation and relative angles of different GRZ sets. Within the transition zone and hornblende-rich body, modified GRZ are variably deformed (Fig. 4a, 5a,b). Here, the intensity of deformation generally increases towards and within the hornblende-rich body (Fig. 5a, b). Strain intensity is observed to be independent from discernible mineralogical differences (i.e. garnet-rich stringers surrounded by felsic or mafic minerals). At both the northern and southern sides of the hornblende-rich body, modified GRZ are deflected when entering the transition zone, suggesting apparent sinistral displacement (Fig. 1b, 5a, b). This deflection in the transition zone is accompanied by deflection and transposition of the S_1 foliation (Fig. 5a). Modified GRZ continue into the hornblende-rich body, now garnetite stringers, where they are variably deformed (Fig. 5a). Within the hornblende-rich body, the observed angles between different garnetite stringers show that strain levels are

highly variable. Some domains show low-strain, where garnetite stringers preserve near-rectilinear patterns, with angles similar to those found in GRZ throughout the Pembroke Valley (compare Figs. 2 & 5e). Open to tight folds of garnetite stringers form symmetric (Fig. 5f) and asymmetric folds (Fig. 5g) and indicate moderate to high-strain. Sheath folds occur in zones interpreted as high-strain zones close to the boundary to the transition zone (Fig. 5h). In these zones, clinozoisite shows a distinct shape preferred orientation (Fig. 5b).

WHOLE ROCK CHEMISTRY

Whole rock XRF chemistry of major element compositions of the host gabbroic gneiss, transition zone and the hornblende-rich body (separated into sub-units as clinozoisite-hornblendite and hornblendite) shows that the host gneiss and the rocks within the transition zone have very similar whole rock chemistry in terms of SiO_2, MgO, Fe_2O_3 and Na_2O except a slight increase (from 0.4 to 0.9) in LOI in the transition zone rocks (Fig. 6). This stands in stark contrast to the clinozoisite-hornblendite and hornblendite rock types which exhibit a marked decrease in silica content and Na_2O, and an increase in MgO and Fe_2O_3 (Fig. 6). Further to this, LOI values of the hornblende-rich body are increased further to 1.4–2.0. Further details regarding whole rock REE patterns are provided by Stuart, Meek, et al. (2018).

DETAILED PETROGRAPHY AND QUANTITATIVE ORIENTATION ANALYSIS OF THE MAIN ROCK TYPES

Clinozoisite-hornblendite

The clinozoisite-hornblendite rock is dominated by green hornblende (up to ~80 area %) and clinozoisite (up to ~50 area %) (Fig. 7a, Table 1). Hornblende grains are subhedral to anhedral and locally display a narrow Gaussian grain size distribution, with a grain size range of 0.5–5 mm and an average grain size around 3 mm. Hornblende is inclusion-free and has no shape preferred orientation (Fig. 7a, b). Clinozoisite grains are elongate, euhedral crystals with

rounded tips, and have a narrow Gaussian grain size distribution between 1–5 mm in length and peak size 2.5 mm. Crystals are no more than 1–3 mm wide with aspect ratios between 2 and 3. Clinozoisite grains regularly have inclusions of rounded green hornblende (<0.05 mm) (Fig. 7a). Some clinozoisite grains have more complex, equidimensional multiphase inclusions of hornblende, plagioclase, clinochlore and K-feldspar (Fig. 7c, d, e). Clinozoisite is commonly randomly orientated (Fig. 3a, c). However, they can also have a distinct shape preferred orientation in higher strain areas (Fig. 5a, b, Fig. 7a).

Plagioclase is a minor mineral (< 5 area %) of the clinozoisite hornblendite. It is found only as small grains along grain boundaries of hornblende, clinozoisite and garnet (in the case of the garnetite stringers) and at triple junctions of the latter (Fig. 7a, b, e, f, h, i). They do not display the rectangular shape typical for euhedral, igneous plagioclase crystals. Instead, they are elongate grains, with pointed ends, with some grains exhibiting low apparent dihedral angles of between <10º—<60° (Fig. 7b, e, f, g, h) giving them an interstitial appearance. There is an abundance of low dihedral angles <60°, however, of particular interest are several very low apparent dihedral angles <10° (Fig. 7f, g). Measurements of apparent low dihedral angles are made using BSE images via ImageJ. A histogram of the apparent angles shows a relatively even spread of angles between <10°—<60° (Fig. S1). Plagioclase grains display no shape preferred orientation. EBSD analyses show that small plagioclase grains at clinozoisite and/or hornblende boundaries are often connected in 3D, even if not connected in 2D (Fig. 7b inset). This is shown by plagioclase grains showing the same crystallographic orientation including twin relationships across several small nearby plagioclase grains (Fig. 7b inset).

Multiphase inclusions within clinozoisite show that clinozoisite hosting the inclusion and the clinozoisite “within” the inclusions have the same crystallographic orientation (Fig. 7e). Within a single inclusion, hornblende and clinochlore each exhibit, per phase, the same crystallographic orientation (Fig. 7 e). Plagioclase also has similar orientations including some

357 twin orientations (Fig. 7e). Within these multiphase inclusions, mineral grain boundaries are
358 interlobate–amoeboid, rarely displaying crystal faces (Fig. 7c-e) where hornblende is seen to
359 have the largest grain size with other minerals being finer grained (Fig. 7d–e).

360 In some cases, plagioclase grains are associated with near circular domains made of a mixture
361 of biotite, hornblende, garnet, apatite and oxides (rutile or ilmenite) (Fig. 7h). Also, in these
362 cases, EBSD analyses confirm the plagioclase to be a single grain, i.e., with the same
363 crystallographic orientation including twin boundaries (Fig. 7i).

364 **Hornblendite**

365 The hornblendite is dominated by green hornblende (~95 area %) (Table 1). Subhedral to
366 anhedral hornblende displays a bimodal grain size distribution (large grains up to 5 mm
367 length/width, with smaller grains >0.5–2 mm) with near equant grains (Fig. 8a). Hornblende is
368 inclusion free and has no shape preferred orientation (Fig. 8a). By definition, less than 10 area
369 % of clinozoisite is present (Table 1). Plagioclase is a minor constituent (<5 area %), present
370 only as distinct highly elongate grains along grain boundaries of hornblende, between 1–5 mm
371 length (Fig. 8a, b). They similarly have pointed tips and commonly display low apparent
372 dihedral angles of <10º (Fig. 8a, b). Plagioclase is generally inclusion-free. However, some
373 plagioclase grains situated at hornblende triple junctions (~650 μm wide) have inclusions of
374 biotite, garnet and oxides (e.g. rutile) (Fig. 8b, c). In this case, plagioclase exhibits highly
375 irregular boundaries, with several boundaries ending in pointed ends, some with very low
376 apparent dihedral angles of <10º (Fig. 8b–d). Euhedral to subhedral, tabular biotite inclusions
377 (50–450 μm length) are randomly orientated within the plagioclase cluster and are found both
378 within the plagioclase as well as in contact with the surrounding hornblende (Fig. 8b). Within
379 these clusters, garnet (50–150μm) is generally rounded with cuspate–lobate grain edges and
380 completely enclosed by plagioclase (Fig. 8b). All garnet grains within the plagioclase cluster

have the same crystallographic orientation (Fig. 8d and inset). However, plagioclase shows two main orientations ignoring their respective twins (Fig. 8d).

Garnetite stringers

Garnetite stringers are present within both clinozoisite-hornblendite and hornblendite; they exhibit the same characteristics in both rock types (Fig. 7a, 8a). Garnetite stringers are comprised predominantly of medium–coarse grained (100–700 μm), inclusion-free garnet (~95 area %) (Fig. 9a–e, Table 1). Garnet grains have highly irregular shapes, interlocking amoeboidal grain boundaries and no shape preferred orientation. Garnet crystallographic orientation data highlight the lack of any crystallographic preferred orientation; e.g. grain orientations have a wide spread (Fig. 9d, pole figure, all data). Within individual grains, sub-grain boundaries (>5–10º misorientation) and irregular intra-grain lattice distortions are seen (Fig. 9d,e, pole figure, blue grain). Both features show a distinct lack of clear dispersion patterns, i.e., small circle dispersions seen in pole figures (Fig. 9d).

Plagioclase (<5 area %, Table 1) within garnetite stringers is present as elongate grains along garnet grain boundaries, with pointed ends, and some ending in very low apparent dihedral angles of <10º (Fig. 9a–c). Plagioclase is sometimes interlocked with hornblende (Fig. 9a–c). Plagioclase around surrounding hornblende grains shows crystallographic continuity (Fig. 9b). Hornblende may exhibit subhedral to anhedral shapes (Fig. 9c).

Transition zone hornblende-feldspar gneiss and its contact with hornblende-rich body rock types

Both hornblendite and clinozoisite-hornblendite are in contact with the transition zone (Figs 1b, 5a–b). This section focusses on the details of the boundary between the transition zone gneiss and hornblendite units. Hornblende grains found at the boundary of the two rock types are finer grained (up to 2mm length) than those found in the hornblende-rich rock types and

405 the gabbroic gneiss (compare Fig. 2b & Fig. 7a, 8a, 10a). At the boundary, hornblende within
406 the hornblendite is inclusion-free and exhibits a weak shape-preferred orientation, similar to
407 the foliation in the transition zone hornblende-feldspar gneiss. As typical for the transition
408 zone, this hornblende-feldspar gneiss is very similar to the two pyroxene-pargasite gneiss (Fig.
409 2b) where elongate clusters of hornblende define the gneissosity within a plagioclase-rich
410 matrix, except hornblende has replaced the two-pyroxene assemblage (Fig. 2a, 10a, Table 1).

411 The boundary between the two rock types is abrupt, with a mineralogical change at a single-
412 grain-scale (Fig. 10a–c). Plagioclase mode decreases from 45 area% in the hornblende-feldspar
413 gneiss of the transition zone to <5 area% in the hornblendite, while hornblende mode increases
414 from 45 area% to >95 area% (Fig. 10a, Table 1). Directly at the boundary, hornblende in the
415 transition zone and within the hornblende-rich body are similar in orientation and size.
416 However, while plagioclase is present as both large (mm sized) porphyroclasts and small,
417 recrystallized grains within the transition zone, at the boundary it is seen as small grains or
418 "partially replaced remnants" surrounded by hornblende (Fig. 10b).

419 The immediate contact boundary is irregular at the grain-scale. Here, hornblende and
420 plagioclase grain boundaries are highly irregular exhibiting a strongly corroded, cuspate-lobate
421 nature (Fig. 10a–c, 10b inset). Plagioclase has a bimodal grain size distribution (Fig. 10b,
422 inset). Larger plagioclase grains (>100 μm) resemble those seen in the transition zone
423 hornblende-feldspar gneiss where they exhibit tapered and bent twins (Fig. 10b). Where
424 plagioclase and hornblende are in direct contact, clusters of smaller grains of plagioclase are
425 present (< 50–100 μm) (Fig. 10b inset). They show no internal deformation features or
426 crystallographic preferred orientation (Fig. 10b). Hornblende also shows a bimodal grain size
427 distribution where large grains are up to 2mm in length and smaller grains of hornblende (<50–
428 100 μm) occur in clusters (Fig. 10c). Plagioclase remnants found within hornblende grains
429 exhibit crystallographic orientations continuous with plagioclase adjacent to the hornblende

grain (arrow on Fig. 10b). Small hornblende grains are seen between plagioclase grains and in rare cases along twin planes (Fig. 10c). Interestingly, hornblende is commonly seen to occur between grain boundaries of large plagioclase grains (Fig. 10b–e), irrespective of twin plane orientation. In rare instances, hornblende is found along sub-grain boundaries of plagioclase (Fig. 10e).

DISCUSSION

The Pembroke Granulite, Fiordland, provides an exceptionally well exposed window into the lower arc crust, and therefore has been extensively investigated in earlier literature in the light of its tectonometamorphic evolution (Blattner, 1976; Bradshaw, 1989a; Bradshaw, 1989b; Clarke, Daczko, Klepeis, & Rushmer, 2005; Clarke et al., 2000; Daczko, Clarke, et al., 2001; Daczko, Clarke, & Klepeis, 2002; Daczko, Klepeis, et al., 2001; Gardner, Piazolo, & Daczko, 2016; Klepeis, Clarke, & Rushmer, 2003; Mortimer et al., 1999; Schröter et al., 2004; Smith et al., 2015; Stevenson, Daczko, Clarke, Pearson, & Klepeis, 2005; Stuart et al., 2017). Different to previous studies, this study focusses on the hornblende-rich bodies, which in earlier studies have not been considered in detail and been referred to as 'ultramafic pods or bodies' (Clarke et al., 2000; Daczko, Clarke, et al., 2001). We discuss below evidence for the protolith of the hornblende-rich body, and likely formation processes. Hornblendites have been shown to form from fractional crystallisation (Jagoutz, Müntener, Schmidt, & Burg, 2011) as well as hydration of gabbroic gneiss igneous protolith (Wade, Dyck, Palin, Moore, & Smye, 2017). We show that while there are several 'igneous-like' characteristics suggesting a potential cumulate fractionation origin (part 1), other features preclude this interpretation (part 2), and instead point to a melt-rock interaction process.

Hornblende-rich body: a late tectonic "igneous body" hosted in an actively deforming zone that cuts a metamorphic terrain

454 We discuss features of the hornblende-rich body typical for an 'igneous-like' body post-dating
455 the main regional tectonometamorphic events. This interpretation is based on three key
456 observations:

457 I. Field relationships suggest that the hornblendite postdates the two earliest
458 tectonometamorphic events in the Pembroke Granulite. The boundaries of the
459 hornblendite cross-cuts the regional S_1 foliation, D_2 formation of garnet reaction zones
460 (GRZ) and D_3 shear zones.
461 II. The hornblende-rich body has an igneous character in terms of cumulate-like
462 mineralogy (up to ~50-95% hornblende), presence of pegmatites that are spatially
463 linked to the hornblende-rich body (Fig. 1b, Fig. 3b) and microstructures indicative of
464 the former presence of melt.
465 III. The whole-rock geochemistry of the hornblende-rich body is distinct from the gabbroic
466 gneiss exhibiting characteristics typical for igneous ultramafic lenses (Fig. 6) (Clarke
467 et al., 2005; Daczko, Klepeis, et al., 2001).

468 The hornblende-rich body is present within the regional gabbroic gneiss which records three
469 early deformation events (D_{1-3}). D_1 is a high temperature tectonometamorphic event, resulted
470 in solid-state crystal plasticity (Fig. 10b, e, Smith et al., 2015). D_2 is recorded by rectilinear
471 dyking, where anhydrous melt infiltrates through a dyke network and reacts with host gneiss,
472 transforming the adjacent rock to garnet granulite in distinct 2–5 cm garnet reaction zones
473 (GRZ) (Blattner, 1976; Clarke et al., 2005; Daczko, Clarke, et al., 2001; Schröter et al., 2004).
474 In contrast, the hornblende-rich body commonly lacks a well-developed foliation, except in
475 high-strain areas, where moderate to strongly developed shape preferred orientations can be
476 seen in both hornblende and clinozoisite (Fig. 1b, Fig.8a, Fig. 10a).

477 Field relationships suggest that the hornblende-rich body is hosted within a post-D_2
478 deformation zone. This is illustrated by systematic bending of the S_1 gneissosity and the pre-

existing D_2 GRZ into the hornblendite body (particularly those oriented perpendicular to the hornblende-rich body–host boundary (Fig. 1b, 5a,b) indicating a component of sinistral shearing (Fig. 1b, 5 a, b). The relative timing of the hornblende-rich body is either syn-deformational with respect to D_3 shear zones, or is post-D_3 deformation (Stuart, Meek, et al., 2018).

Furthermore, within the hornblende-rich body, strain variation is apparent: (i) anastomosing near pure hornblendite areas are seen within a predominantly hornblende-clinozoisite rock and are oriented subparallel to the transition zone – hornblende-rich body boundary (Fig. 1b) and (ii) simple folding and stretching to sheath folding of modified GRZ are common within the hornblendite-rich body (Fig. 5e-h). The consistency of displacement structures at the contact between the host gneiss and the hornblende-rich body, and parallelism of structures within the body with body boundaries suggests an external stress regime causing sinistral shearing associated with hornblende-rich body formation.

The locally near-chaotic folding suggests that some volume loss occurred, however, the continuity of GRZ from outside to within the hornblende-rich body precludes high volume losses which would result in disjunct collapse structures (Bons, Druguet, Castaño, & Elburg, 2008) or avalanches of instabilities with hydrofractures (Bons et al., 2004).

Microstructures related to the *former* presence of melt in a rock have been widely characterised and a set of criteria agreed upon in the literature. They have been characterised extensively in migmatites (Hasalová, Schulmann, et al., 2008a; Holness & Sawyer, 2008; Vernon, 2011) and cumulate rocks (Holness, Cheadle, & McKenzie, 2005; Holness, Clemens, & Vernon, 2018). Key microstructures include: 1) interstitial, often monomineralic films present along grain boundaries (e.g. hornblende and/or garnet, Figs 7b, h, Fig. 8b, Fig. 9a), 2) low dihedral angles (<60º) of minerals representing pseudomorphs of former melt in equilibrium with solid

503 minerals (e.g. plagioclase, Figs 7b, f, g, h, Fig. 8b, Fig. 9a), 3) irregularly shaped pockets
504 (cuspate-lobate or embayed boundaries) commonly containing blocky, euhedral minerals
505 inferred to have grown from the melt (e.g. Fig. 7h, i, Fig. 8b–d), 4) neoblasts growing into
506 indentations (embayments) of melt-filled boundaries (e.g. plagioclase neoblasts interpreted to
507 represent pseudomorphed interconnected 3D melt networks (Fig. 7b, inset, Fig. 9b)), and 5)
508 mineral growths with orientations sub-perpendicular or perpendicular to neighbouring minerals
509 (Hasalová, Schulmann, et al., 2008a; Holness, 2006; Holness & Sawyer, 2008; Marchildon &
510 Brown, 2002; Sawyer, 1999; Sawyer, 2001; Vernon, 2011). Although these textures are used
511 to identify the former presence of a melt at some point in the rocks' geological history, they
512 are rarely linked to melt-rock interaction and/or melt movement through a host rock.
513 Consequently, linking microstructures indicative of the former presence of melt to the
514 mechanisms of pervasive melt migration and porous melt flow replacement reactions is
515 desirable.

516 The dihedral angle of a melt between two solid minerals has a primary control on the
517 permeability of the rock and hence, controls the connectivity of melt distribution and enhances
518 melt migration (Holness, 2006; Vernon, 2011). Therefore, melt-solid-solid dihedral angles of
519 60º or less have been shown to allow interconnected melt networks to flow in geological
520 systems (Holness, 2006), as opposed to isolated melt-filled pores (>60º) which stagnates melt
521 and prevents flow. During cooling, melt will solidify into these pore networks, and
522 pseudomorph the pore space used during melt movement (Hasalová, Schulmann, et al., 2008a;
523 Holness, 2006; Sawyer, 2001; Vernon, 2011). In the studied system, apparent dihedral angles
524 are as low as 10º (Fig. 7b, f, g, h, 8b, 9a).

525 When melt-solid-solid dihedral angles approach zero, grain boundary melt films are
526 pseudomorphed by highly elongate grains of the interstitial phase along grain boundaries
527 (Rosenberg & Riller, 2000). Hence, films of primarily plagioclase (Fig. 7b, f, g, h, 8b, 9a, and

528 in rarer instances, hornblende, Fig. 7h, 9a-c) along grain boundaries of hornblende, clinozoisite
529 and garnet, are interpreted to indicate pseudomorphs of grain boundary melt networks. Pore
530 spaces bound by fewer than four surrounding solid grains will typically be pseudomorphed by
531 single grains (i.e. plagioclase in this example; Hasalová et al 2008). However, as pore size
532 increases between solid grains, so does the ability of polymineralic aggregates to crystallize.
533 Multiphase crystal aggregates (biotite, garnet, apatite, rutile in this study) hosted within single
534 plagioclase grains are interpreted to indicate late stage crystallization of melt-filled pores
535 during cooling (Fig. 7h, i, Fig. 8b-d) (Holness & Sawyer, 2008; Sawyer, 2001). As plagioclase
536 crystallizes (generally 1–2 main grains depending on the pore size), other minerals are able to
537 crystallize from the melt composition, leading to multiphase crystal aggregates that replace
538 former melt pockets (Holness & Sawyer, 2008).

539 Discontinuous films of interstitial plagioclase along grain boundaries, are sometimes shown to
540 be connected in 3D (due to their single, consistent twin set orientations) even when not
541 connected in 2D (Fig. 7b, inset, Fig. 9b). These results are consistent with melt crystallizing
542 and pseudomorphing an interconnected melt porosity (Holness & Sawyer, 2008) forming an
543 interstitial texture. Low nucleation rates are also likely to play a role (Vernon, 2004).

544 The very coarse grained pegmatitic patches are only seen within the hornblende-rich body (Fig.
545 1b, Fig. 3b). These are characterized by typical igneous textures with plagioclase as an
546 interstitial mineral (Fig. 3b). This, along with the fact that these pegmatitic bodies have very
547 diffuse, irregular boundaries and comprise the same mineral assemblage as the rest of the
548 hornblende-rich body suggests that the pegmatite is part of the hornblende-rich body.
549 Consequently, these pegmatites are likely to represent the accumulation and final precipitation
550 of the melt associated with the formation of the hornblende-rich body, as late-stage low
551 pressure zones. In summary, the abundant microstructures indicative of the former presence of

552 melt and pegmatitic bodies within the hornblende-rich body are consistent with an igneous
553 origin.

554 **Hornblende-rich body: A product of melt-rock interaction involving melt-mediated**
555 **reactions**

556 Field relationships indicate that the hornblende-rich body cannot have intruded as a dyke or
557 hydrofracture into the pre-existing two-pyroxene-pargasite gneiss as there is no definitive or
558 clear structural break between the different rock types. Furthermore, the continuity and
559 modification of previously existing GRZ from the host gneiss through the transition zone into
560 the hornblende-rich body necessitates the hornblende-rich body to be a product of extreme
561 modification of the host gneiss (Daczko et al., 2016). This modification must have occurred *in*
562 *situ* to enable the observed structural continuity (Fig. 4a, b, 5c, d). Porphyroblastic growth of
563 euhedral garnet (some with surrounding feldspar rich rims, see Fig. 3d inset) are common
564 within the transition zone, particularly close to the contact of the hornblende-rich body, as well
565 as within the hornblende-rich body and pegmatite domains (Fig. 3b-d). These large euhedral
566 garnets point to the growth of minerals in the presence of a melt (Stuart et al., 2017). The
567 leucosome material closely associated with these euhedral garnets (Fig. 3d inset) are consistent
568 with felsic pseudomorphs after melt (Stuart et al. 2017).

569 Microstructures within the hornblende-rich body show unequivocally that it formerly contained
570 melt and that the microstructural development is closely related to reactive melt-rock
571 interactions and melt crystallisation. This is particularly clear at the contact boundary between
572 the transition zone and the hornblende-rich body where microstructures are consistent with
573 plagioclase being dissolved and replaced by hornblende (Fig. 10b–e). Boundaries between
574 plagioclase and hornblende are highly irregular. Orientation mapping shows the older, remnant
575 plagioclase of the gabbroic gneiss retains deformation twinning, while newly grown

576 hornblende shows no evidence of high-grade solid-state deformation (Fig. 10b). As strained
577 crystal lattices and deformation twinning are typical in the host gneiss and absent within the
578 hornblendite body, the hornblendite is post-tectonic (post-S_1). The remnants of old plagioclase
579 within newly formed hornblende grains at the hornblendite–transition zone boundary are
580 interpreted to reflect a disequilibrium texture, where the plagioclase was unstable and dissolved
581 to produce hornblende. We suggest that this disequilibrium was induced by interaction with an
582 externally-derived reactive melt. At the contact between a reactive melt and the pre-existing
583 two-pyroxene-pargasite gneiss, coupled dissolution-precipitation replacement reactions
584 occurred (Putnis, 2009). In such reactions, the phase that is chemically unstable (i.e.
585 undersaturated within the fluid/melt) is dissolved into the fluid/melt and the phase that is
586 oversaturated with respect to the fluid grows (Spruzeniece, Piazolo, Daczko, Kilburn, & Putnis,
587 2017). If these processes are coupled, the new phase replaces the volume occupied by the
588 dissolving phase (Putnis, 2009). If this process occurs in an open fluid system, the original
589 material will show a marked decrease in the abundance of the unstable phase and an increase
590 in the stable phase. In our example, modal percentages (Table 1) of plagioclase and hornblende
591 of the host gneiss (45, 20% respectively, with 25% pyroxenes present), moderately change in
592 the transition zone (45, 45% respectively, pyroxenes absent) before dramatically changing in
593 the hornblende-rich body (<5, up to 95% respectively), as a result of melt-mediated
594 replacement reactions within an open system. Interestingly, plagioclase twin boundaries appear
595 to have no influence on melt infiltration or reaction, as we do not see any preferred plagioclase
596 dissolution and hornblende crystallization along these twins (Fig. 10a-e).

597 Within the hornblende-rich body, hornblende grains exhibit subhedral to anhedral grain shapes,
598 with some euhedral crystal faces; whereas, clinozoisite exhibits euhedral grain boundaries with
599 poikilitic structures, similar to a weakly ophitic texture caused by low nucleation rates (Vernon,
600 2004). Neither mineral exhibits compositional zoning. We interpret these features may indicate

601 rapid growth within a confined space after nucleation, or sparse nucleation within a melt-
602 present system. Garnet grains within garnetite stringers exhibit unusual amoeboid grain shapes,
603 which we also interpret to occur due to melt-mediated reactions (Figs 9d, e). We infer that
604 garnetite stringers are where melt has reacted with and intensely modified pre-existing GRZ.
605 In this case, the melt dissolves plagioclase and pyroxene from GRZ and replaces these with
606 garnet, forming amoeboid garnet grain shapes. Of note are the frequent subgrain boundaries
607 and lattice distortions within the garnet (Fig. 9d, e). Further to this, garnetite stringers are
608 corroded and warped by melt-rock reactions, associated strain and deformation, and are
609 therefore significantly thinner within the hornblende-rich body compared to the width of the
610 original GRZ (Figs 2a versus Figs 5e-h). In summary, we suggest that these features are a
611 product of rapid replacement reactions which are found to be similar to the microstructures
612 formed during experimental fluid-mediated replacement reaction in salts (Spruzeniece,
613 Piazolo, & Maynard-Casely, 2017).

614 Our microstructural observations at the boundary between the hornblende-rich body and the
615 transition zone demonstrate that the host gneiss reacted with the melt, in the following reaction
616 involving reactive flow of an externally-derived melt: Cpx + Opx + Pl + $melt_1$ → Hbl ± Cz ±
617 Grt + $melt_2$. Relevant melt-rock reaction experiments are lacking and are needed to explore
618 these processes. However, igneous phase equilibria experiments investigating the stabilities of
619 ferromagnesian silicates (pyroxene, hornblende, clinozoisite, biotite) and plagioclase (+ quartz)
620 within H_2O-rich granodioritic melt (8–11 wt.% H_2O), indicate that these minerals are co-stable
621 within T= ~675–720 ºC at 8 kbar (Naney, 1983), possibly pointing toward an intermediate
622 composition melt being involved in the formation of the clinozoisite-bearing hornblendite
623 rocks. Other experiments that investigated phase equilibria for gabbroic and andesitic melts
624 (with up to ~5 wt. % H_2O) found that the addition of water depresses the solidus and liquidus
625 of the system and increases the stability of hydrous minerals (Green 1982). This is consistent

626 with our interpretation that melt-mediated replacement reactions can occur between rocks with
627 little chemical variation (i.e. hydrous gabbroic melt reacting with gabbroic rock may form
628 hornblendite at high-T conditions near the liquidus of the hydrous melt).

629 Hornblende in this study is pargasite amphibole (Stuart, Meek, et al., 2018) which is known to
630 be a high P-T amphibole (Niida & Green, 1999). The abundance of clinozoisite within the
631 hornblende-rich body, with euhedral crystal faces and abundant pargasite hornblende
632 inclusions suggests they crystallised together (Figure 7a). Although clinozoisite is found
633 regularly in lower temperature epidote-amphibolite facies, numerous studies, both
634 experimental (Johnston & Wyllie, 1988; Naney, 1983) and in natural samples (Evans & Vance,
635 1987; Zen & Hammarstrom, 1984) have shown that it can also form magmatically at higher
636 pressures and temperatures (Schmidt & Poli, 2004). Textural criteria are established to infer
637 magmatic epidote: (i) euhedral to subhedral grain shapes with clear grain boundaries and (ii)
638 mineral associations with primary hornblende (Pandit, Panigrahi, & Moriyama, 2014). Primary
639 magmatic clinozoisite has also been identified petrographically in ultramafic rocks where
640 euhedral grains consist of inclusions of hornblende (and minor garnet), as is similar to our case
641 (Bazylev, Ledneva, Kononkova, & Ishiwatari, 2013). Geochemically, pistacite (Ps) content is
642 used to attempt and distinguish magmatic from metamorphic epidote. However, this has not
643 proven to be a useful indicator due to indistinguishable data (Schmidt & Poli, 2004). In
644 contrast, rare earth element patterns have been shown to be distinct for igneous versus
645 metamorphic epidote and the clinozoisite grains in the hornblende-rich body of this study have
646 rare earth element patterns consistent with them being of igneous origin (Stuart et al., 2018b).

647 The composition of the fluxing melt was likely a hydrous granodioritic to gabbroic magma.
648 This conclusion is consistent with the mineralogical assemblage found in the hornblende-rich
649 body (hornblende and clinozoisite) and the melt pockets (plagioclase-hosted with
650 crystallizations of biotite, garnet, hornblende, apatite and oxides) as well as the mineral

651 assemblage of plagioclase, hornblende, garnet and clinozoisite observed in the pegmatitic
652 bodies. Our results also agree with experimental data (i.e. Naney, 1983; Green, 1982). A
653 granodioritic to gabbroic magma is also more probable as mafic melts have lower viscosities
654 (Lesher & Spera, 2015; Shaw, 1972). The presence of co-existing garnet and biotite within
655 some melt pockets may indicate either simultaneous crystallization from a possible
656 granodioritic composition or may show a late-stage back-reaction of garnet and melt to biotite
657 (Fig. 8b–e).

658 To summarize, we suggest that the influx of an externally-derived, hydrous silicate melt of
659 varying granodioritic to gabbroic composition, has induced melt-mediated coupled dissolution-
660 precipitation replacement reactions, replacing an anhydrous gabbroic gneiss and GRZ. In this
661 scenario, where the reacting melt infiltrates at the grain-scale, pyroxene and plagioclase react
662 with the melt and are dissolved, preferentially along grain and sub-grain boundaries (Fig. 10b,
663 e, Fig. 11). At the same time, hornblende with or without clinozoisite and garnet precipitate *in*
664 *situ* (Fig. 10c, e, Fig. 11) forming a coupled dissolution-precipitation reaction (Putnis, 2009).
665 Hornblende growth is seen along grain and sub-grain boundaries of plagioclase (Fig. 10c, e)
666 (Levine, Mosher, & Rahl, 2016) resulting in remnants or "islands" of plagioclase within an
667 undeformed hornblende grain (Fig. 10b, c). The observation of finer grained hornblende at the
668 transition zone-hornblendite boundary suggests there is high reaction affinity and a strong
669 driving force to nucleate hornblende in place of plagioclase. In contrast to relatively rapid
670 heating, as seen in contact aureoles, high reaction affinity and overstepping reactions can also
671 be produced by extreme chemical disequilibrium (Roselle, Baumgartner, & Chapman, 1997).
672 Small plagioclase grains are also found, suggesting that locally the melt composition changes
673 and/or connectivity to the open system is hindered, resulting in local re-precipitation of fine-
674 grained plagioclase (Fig. 10b, Fig. 11). Similarly, garnet grows within the pre-existing GRZ.

675 Here plagioclase is dissolved but garnet grows as pre-existing garnet likely acts as easy
676 nucleation sites. Hence, local kinetics must govern their growth.

677 Evidence of both high-variance hornblende-only and hornblende-clinozoisite-rich areas
678 suggests melt-mediated metasomatism (Korzhinskiĭ, 1959) involving variable melt
679 compositions, which occurred due to an evolving melt composition from progressive melt-rock
680 reactions and/or a change in temperature regimes. Clinozoisite-rich areas are likely later in the
681 progression of evolving melt compositions or P-T changes, where clinozoisite nucleates within
682 predominantly hornblende-rich body, replacing hornblende with euhedral grains. This is a more
683 likely scenario than forming epitaxial clinozoisite grains on hornblende.

684 **Deformation-assisted, channelized reactive porous melt flow: a mechanism of mass**
685 **transfer within the lower arc crust**

686 Successful melt-mediated replacement reactions require an efficient process for melt
687 migration, otherwise the reaction will stall (Jonas, Müller, Dohmen, Baumgartner, & Putlitz,
688 2015). In other words, if the reactive melt cannot access the reactive host rock, no reaction can
689 take place. We propose that the mechanism facilitating melt migration and open system
690 behaviour involves pervasive melt movement along grain boundaries during deformation in a
691 shear zone. During melt-present deformation, melt infiltrates along grain boundaries and within
692 triple junctions, forming an interconnected, highly permeable network of melt movement (Scott
693 & Stevenson, 1986; Turcotte & Ahern, 1978). This mechanism of porous melt flow is
694 commonly invoked for lower strain formation of mantle melt conduits, as well as transporting
695 melt through focused channels within the mantle (Dijkstra et al., 2003; Kelemen et al., 1995).
696 In these scenarios, the viscosity and density contrast between host rock and migrating melt are
697 larger compared to within the Earth's crust. Our study suggests that a similar mechanism is an
698 important process of pervasive melt migration through generally anhydrous lower arc crust but

699 requires accompanying deformation to proceed. For porous melt flow to be effective, there
700 must be a driving force for melt migration and pathways, i.e. porosity that does not close as a
701 result of the melt-rock reaction and a permeable interconnected network. Porosity and
702 permeability are likely to be maintained during ongoing deformation.

703 Movement of melt via porous flow can be, in principle, buoyancy-driven (Solano et al., 2012),
704 or stress-driven via deformation (Hasalová, Schulmann, et al., 2008a). In situations where
705 deformation-assisted melt percolation occurs (e.g. in shear zones), porosity is dynamically
706 produced (Fusseis, Regenauer-Lieb, Liu, Hough, & De Carlo, 2009; Hasalová, Schulmann, et
707 al., 2008a). If the migrating melt is mafic and has a high water content, porous melt flow is
708 easier to achieve, as elevated water contents lower melt viscosity by several orders of
709 magnitude (Richet, Lejeune, Holtz, & Roux, 1996; Shaw, 1972; Stuart et al., 2016). At the
710 same time, hydrous melt would result also in a decrease of the dihedral angle between minerals
711 and melt allowing better grain-scale connectivity (Fujii, Osamura, & Takahashi, 1986). Still,
712 the density contrast between the host rock and melt may not be sufficiently large to allow
713 buoyancy-driven porous melt flow in the crust. Hence, the necessary additional factor enabling
714 significant porous melt flow in the lower arc crust is deformation (Hasalová, Schulmann, et al.,
715 2008a). In our case, the fact that the reactive melt must have been mafic–intermediate, hydrous
716 and occurred in a shear zone, supports the interpretation that a combination of buoyancy and
717 deformation-driven porous melt flow facilitated melt migration. Here, sinistral shearing (as
718 seen by the deflection of GRZ into the transition zone and hornblende-rich body in the field,
719 Fig. 1b, Fig. 5a, b) has resulted in dynamic porosity generation and therefore assisted porous
720 melt flow through the system; this allowed reactions to occur geologically fast.

721 We suggest that the melt-rock reaction occurred dominantly at grain boundaries. In the case of
722 a coupled dissolution-precipitation replacement reaction, dissolution of the unstable phases
723 will create porosity and therefore permeability, further allowing the migrating melt to move

724 through the constantly evolving grain boundary networks (Kelemen et al., 1995). Similar to
725 scenarios advocated for e.g. dunite channel production in the mantle (Braun & Kelemen, 2002),
726 minerals in equilibrium with the melt will not only nucleate and grow, but importantly
727 dissolution of minerals creates space, allowing the process to occur *in situ*. The dissolution-
728 precipitation process increases permeability and helps drive a continuous melt flux through the
729 system. Volume changes involved in melt-rock interactions may additionally create space or
730 increase melt fluid pressure, resulting in fracturing and further reaction (Jamtveit, Putnis, &
731 Malthe-Sørenssen, 2009).

732 The model of melt-mediated dissolution-precipitation replacement reactions presented here,
733 closely resembles field and experimental studies on mantle rocks. As such, several studies have
734 characterized the formation of dunite (Ol) (Kelemen et al., 1995; Morgan & Liang, 2003; Pec,
735 Holtzman, Zimmerman, & Kohlstedt, 2017), lherzolite (Ol + Opx + Cpx) (Morgan & Liang,
736 2005) and harzburgite (Ol + Opx) (Kelemen et al., 1992) via reaction with a silica over- or
737 under-saturated melt. Typically, the composition of the melt that migrates through a host rock,
738 the composition of the host rock (i.e. mantle peridotite), and P-T conditions dictates which
739 minerals will dissolve and precipitate. For mantle conditions, this process is thought to be
740 initiated by geochemical melt compositions (basalt or fractionated versions thereof)
741 significantly different to the host rock compositions (peridotite, dunite, harzburgite). The vast
742 geochemical differences can easily initiate chemical disequilibrium, as there are large
743 differences in the relative solubility of the dissolving versus precipitating minerals in the melt
744 that will drive melt-mediated replacement reactions. Interestingly, field studies of these
745 processes in mantle rocks (Kelemen et al., 1995) show the same angular remnants or "islands"
746 of un-reacted host material within the reacted zones as we observe in our field example of lower
747 crust (Fig, 1b, Fig. 4e, f).

In summary, we propose the development of the melt flux zone to occur in the following way, (i) an influx of an externally-derived, hydrous silicate melt (of approximate gabbroic to granodioritic composition) into the anhydrous gabbroic gneiss occurs during high-strain deformation, (ii) melt migrates via porous melt flow along grain boundaries, (iii) the melt is reactive with the host gneiss and dissolves pyroxene and plagioclase, starting at grain or sub-grain boundaries (Levine et al., 2016) (Fig. 11), (iv) this increases porosity and permeability, enhancing large volumes of melt flow through the system, (v) hornblende (± clinozoisite, garnet) replaces pyroxene/plagioclase *in situ* via a coupled dissolution-precipitation replacement-reaction (Fig. 11), which is dependent on the stability regime of minerals involved and melt composition, (vi) the reaction occurs preferentially at grain and subgrain boundaries where transport is fastest until the mineral is completely replaced; this results in cuspate-lobate and embayed reaction fronts at the melt-grain interface, (vii) the growing minerals may form some igneous-like crystal facets, (viii) as the melt-rock interactions mature, the melt flow is focused into a channel-like structure which become chemically armoured where the migrating melt is no longer in contact with the host gabbroic gneiss. This results in the arrest of further melt-rock interaction at the observed structural level and the unreactive flow of the melt through the armoured channel (Daczko et al., 2016).

Geochemical studies comparing the “host” and “reacted” rock types formed from crustal porous melt flow have shown little to no chemical differences between the identified rock types, which has been suggested as evidence for low melt fractions (Hasalová, Schulmann, et al., 2008a; Stuart, Meek, et al., 2018; Stuart et al., 2016). In our example, the hornblende-rich body is interpreted to have formed by extensive reactive modification of the enclosing anhydrous gabbroic gneiss, surrounded by a transition zone ‘halo’, where pyroxene grains have reacted to hornblende (Daczko et al., 2016). We interpret the hornblendite to indicate high time-integrated volumes of melt flux and melt-rock interactions that have run to completion,

773 due to the lack of any precursor rock found within main hornblende-rich body, with the
774 exception of isolated remnants of the transition zone (Stuart, Meek, et al., 2018). These
775 remnants, along with the surrounding transition zone, are characterized by a lack of pyroxene
776 and the growth of peritectic garnet with leucosome, and these features indicate lower melt-rock
777 interactions compared with the main hornblende-rich body.

778 Our study shows that the presence of hornblende-rich rocks does not necessitate a cumulate
779 origin. Instead, hornblendite rocks may be produced by melt transfer and melt-mediated
780 replacement reactions. Furthermore, reaction softening by growth of rheologically "soft"
781 minerals (in our case, hornblende and clinozoisite) (Brodie & Rutter, 1985) is shown by
782 garnetite stringers deflecting around transition zone remnants in the hornblende-rich body (see
783 Fig. 4f) and alignment of clinozoisite in folded garnetite stringers (Fig. 5b). However, once
784 melt flux stops, remnant melt will crystalize and locally cause rheological hardening (Prakash
785 et al., 2018). Hence, softening may be intermittent and upon cooling and crystallisation of the
786 melt, the zone is likely to be preserved as subsequent deformation will localize in rheologically
787 softer domains (Diener & Fagereng, 2014; Gardner, Piazolo, Evans, & Daczko, 2017). The
788 recognition that hornblende-rich bodies and their surrounding (e.g. hydrated neighbouring
789 rocks) may be formed by melt-rock interaction has important implications for the interpretation
790 of geochronological data derived from these rocks. For example, Langone et al. (2018) showed
791 that melt-rock (and fluid-rock) interactions affect zircon geochronology by altering mineral
792 isotopic and REE-element compositions and the ages derived from such rocks.

793 Nonetheless, our model is applicable to mafic bodies hosted within lower arc crustal
794 environments (ancient and present) as we invite the re-evaluation of igneous-like bodies that
795 may have formed by a similar mechanism to the hornblende-rich body in this study. We provide
796 field and microstructural criterion that can be used to identify the origin of such bodies.
797 Geochemical signatures are provided in a separate contribution (Stuart, Meek, et al., 2018). We

798 suggest this mechanism is applicable to hot, mafic crust that may be fluxed by hydrous melts
799 of almost similar composition, where melt moves via porous melt flow. We show that hydrous
800 versus anhydrous compositions can provide enough disequilibrium to initiate grain-scale melt-
801 rock reactions.

802 **How to recognise zones of former melt flux in lower crustal terranes**

803 In conclusion, we propose the following features of field, microstructural, and whole rock
804 chemical characteristics as indicative for mass melt transfer within lower arc crust. Field
805 observations show a body with a high variance assemblage with igneous features within a
806 metamorphic rock. However, different to a dyke, the body does not crosscut structural features
807 but instead results in significant yet progressive changes in mineral assemblage and bulk
808 composition. Specifically, field signatures of such melt flux include (i) finger-like apophyses
809 or highly irregular contact boundaries, formed via melt-mediated, coupled dissolution-
810 precipitation replacement reactions and associated localized porosity generation, (ii) the
811 occurrence of a hydrated halo (i.e. transition zone), triggering partial replacement and localized
812 partial melting evidenced by growth of peritectic minerals i.e. porphyroblastic euhedral garnet
813 surrounded by leucosome, (iii) modification of pre-existing features (if available, such as
814 previous dykes), in mineralogy, shape, orientation, etc., and the loss or addition of minerals
815 while preserving their structural continuity, (iv) presence of pegmatite components that shows
816 evidence of syn-deformational emplacement, (v) remnant bodies of less reacted sections of
817 original host rock within the hornblende-rich body. Whole rock chemistry of the zone of former
818 melt flux is distinct from that of host rocks, even when structural continuity can be seen
819 between the rock types. Within the zones of former mass transfer, microstructures indicating
820 the former presence of melt include (i) elongate films along grain boundaries, (ii) melt pockets
821 (iii) low dihedral angles <60º, as well as 3D melt network connectivity seen from orientation
822 mapping indicates the ability of the melt to flow within a system. Reaction microstructures

including (i) instability fronts between reacting minerals, where heavily cuspate-lobate or amoeboid grain boundaries show evidence of disequilibrium, allowing dissolution of unstable minerals to occur, and precipitation or replacement by stable minerals, (ii) lattice distortion with no systematic orientation (i.e. stress, strain, deformation) indicating melt-mediated replacement reactions, and (iii) irregular grain boundaries and "remnants" of old grains within new grains, indicate melt-rock interactions. These signatures, along with high melt fractions (as seen in this case) have allowed the reaction to run to completion. As the underlying process of melt-mediated replacement reactions occurs exceptionally fast and in a confined space, crystal shapes will not be euhedral, but have some subhedral to anhedral crystal faces, and limited compositional zoning develops if the geochemistry of the fluxing melt remains relatively similar throughout the event.

In this present work, we concentrate on an example of deformation-assisted migration of a hydrous mafic melt through relatively anhydrous mafic arc crust. However, similar microstructures and reaction textures should be expected in more felsic, granitic orogenic lower crustal systems of melt transfer, though reaction products and interstitial minerals will be different. We suggest that in regions where melt networks are pre-existing and/or where deformation forms pressure gradients and facilitates permeable connection with a melt source, pervasive melt flow could proceed. As mineral stabilities are dependent on the externally derived melt composition and the host rock composition, as well as the P-T conditions of the system, we suggest that biotite will be an important product of hydration crystallisation reactions in felsic systems. The interstitial minerals are also likely to involve quartz and/or K-feldspar, in addition to plagioclase. The interested reader is pointed to research focussing on the rheology of felsic granitic systems with interstitial melt flow (Hasalová, Janoušek, Schulmann, Štípská, & Erban, 2008b; Hasalová, Schulmann, et al., 2008a; Hasalová, Štípská,

et al., 2008c; Schulmann et al., 2008; Štípská et al., 2019; Závada, Schulmann, Konopásek, Ulrich, & Lexa, 2007; Závada et al., 2018).

Understanding this process allows for better understanding of lower crustal rheology; where deformation assisted, channelized reactive melt flow produces a transient rheologically soft unit, where post-crystallization and post-melt flux hardening allows preservation of mass melt transfer conduits and their delicate microstructures.

ACKNOWLEDGEMENTS

ARC Future Fellowship (FT110100070) to SP and Discovery Project funding (DP120102060) to SP and NRD provided financial support to conduct this research. We thank the Department of Conservation, New Zealand for permission to visit and sample localities in the Fiordland National Park. Johann Diener, Brendan Dyck and an anonymous reviewer are thanked for careful reviews. We also thank Michael Brown for editorial handling. This is contribution XXX from the ARC Centre of Excellence for Core to Crust Fluid Systems (www.ccfs.mq.edu.au) and XXX from the GEMOC Key Centre (www.gemoc.mq.edu.au).

REFERENCES

Aharonov, E., Whitehead, J., Kelemen, P., & Spiegelman, M. (1995). Channeling instability of upwelling melt in the mantle. *Journal of Geophysical Research: Solid Earth, 100*(B10), 20433-20450.

Allibone, A., Jongens, R., Turnbull, I., Milan, L., Daczko, N. R., DePaoli, M., & Tulloch, A. (2009). Plutonic rocks of western Fiordland, New Zealand: field relations, geochemistry, correlation, and nomenclature. *New Zealand Journal of Geology and Geophysics, 52*(4), 379-415.

Bazylev, B. A., Ledneva, G. V., Kononkova, N. N., & Ishiwatari, A. (2013). High-pressure ultramafics in the lower crustal rocks of the Pekul'ney complex, central Chukchi Peninsula. 1. Petrography and mineralogy. *Petrology, 21*(3), 221-248. doi:10.1134/s0869591113030028

Beach, A., & Fyfe, W. S. (1972). Fluid transport and shear zones at Scourie, Sutherland: Evidence of overthrusting? *Contributions to Mineralogy and Petrology, 36*(3), 175-180. doi:10.1007/bf00371429

877 Bercovici, D. (2003). The generation of plate tectonics from mantle convection. *Earth and*
878 *Planetary Science Letters, 205*(3), 107-121. doi:https://doi.org/10.1016/S0012-
879 821X(02)01009-9
880 Bestmann, M., & Prior, D. J. (2003). Intragranular dynamic recrystallization in naturally
881 deformed calcite marble: diffusion accommodated grain boundary sliding as a result of
882 subgrain rotation recrystallization. *Journal of Structural Geology, 25*(10), 1597-1613.
883 doi:https://doi.org/10.1016/S0191-8141(03)00006-3
884 Blattner, P. (1976). Replacement of hornblende by garnet in granulite facies assemblages near
885 Milford Sound, New Zealand. *Contributions to Mineralogy and Petrology, 55*(2), 181-
886 190. doi:10.1007/bf00372225
887 Blattner, P. (1991). The north Fiordland transcurrent convergence. *New Zealand Journal of*
888 *Geology and Geophysics, 34*(4), 533-542.
889 Bons, P. D., Arnold, J., Elburg, M. A., Kalda, J., Soesoo, A., & van Milligen, B. P. (2004).
890 Melt extraction and accumulation from partially molten rocks. *Lithos, 78*(1-2), 25-42.
891 Bons, P. D., Druguet, E., Castaño, L.-M., & Elburg, M. A. (2008). Finding what is now not
892 there anymore: Recognizing missing fluid and magma volumes. *Geology, 36*(11), 851-
893 854. doi:10.1130/G24984A.1
894 Bradshaw, J. (1989a). Early Cretaceous Vein-Related Garnet Granulite in Fiordland,
895 Southwest New Zealand: A Case for Infiltration of Mantle-Derived-Rich Fluids. *The*
896 *Journal of Geology, 97*(6), 697-717.
897 Bradshaw, J. (1989b). Origin and metamorphic history of an Early Cretaceous polybaric
898 granulite terrain, Fiordland, southwest New Zealand. *Contributions to Mineralogy and*
899 *Petrology, 103*(3), 346-360.
900 Bradshaw, J. (1990). Geology of crystalline rocks of northern Fiordland: details of the granulite
901 facies Western Fiordland Orthogneiss and associated rock units. *New Zealand Journal*
902 *of Geology and Geophysics, 33*(3), 465-484.
903 Braun, M. G., & Kelemen, P. B. (2002). Dunite distribution in the Oman ophiolite: implications
904 for melt flux through porous dunite conduits. *Geochemistry, Geophysics, Geosystems,*
905 *3*(11), 1-21.
906 Brodie, K., & Rutter, E. (1985). On the relationship between deformation and metamorphism,
907 with special reference to the behavior of basic rocks *Metamorphic reactions* (pp. 138-
908 179): Springer.
909 Brown, M. (2010). Melting of the continental crust during orogenesis: the thermal, rheological,
910 and compositional consequences of melt transport from lower to upper continental
911 crustThis article is one of a selection of papers published in this Special Issue on the
912 the theme Lithoprobe—parameters, processes, and the evolution of a continent.
913 *Canadian Journal of Earth Sciences, 47*(5), 655-694. doi:10.1139/E09-057
914 Carter, K. E., & Dworkin, S. I. (1990). Channelized fluid flow through shear zones during
915 fluid-enhanced dynamic recrystallization, Northern Apennines, Italy. *Geology, 18*(8),
916 720-723. doi:10.1130/0091-7613(1990)018<0720:cfftsz>2.3.co;2
917 Cartwright, I., & Barnicoat, A. C. (2003). Geochemical and stable isotope resetting in shear
918 zones from Täschalp: constraints on fluid flow during exhumation in the Western Alps.
919 *Journal of Metamorphic Geology, 21*(2), 143-161. doi:10.1046/j.1525-
920 1314.2003.00423.x
921 Cashman, K. V., Sparks, R. S. J., & Blundy, J. D. (2017). Vertically extensive and unstable
922 magmatic systems: A unified view of igneous processes. *Science, 355*(6331).
923 doi:10.1126/science.aag3055
924 Chapman, T., Clarke, G., & Daczko, N. (2016). Crustal differentiation in a thickened arc—
925 evaluating depth dependences. *Journal of Petrology, 57*(3), 595-620.

926 Chapman, T., Clarke, G., Piazolo, S., & Daczko, N. (2017). Evaluating the importance of
927 metamorphism in the foundering of continental crust. *Scientific Reports, 7*(1), 13039.
928 Clarke, G., Daczko, N., Klepeis, K., & Rushmer, T. (2005). Roles for fluid and/or melt
929 advection in forming high-P mafic migmatites, Fiordland, New Zealand. *Journal of*
930 *Metamorphic Geology, 23*(7), 557-567.
931 Clarke, G., Fitzherbert, J., Milan, L., Daczko, N., & Degeling, H. (2010). Anti-clockwise P–T
932 paths in the lower crust: an example from a kyanite-bearing regional aureole, George
933 Sound, New Zealand. *Journal of Metamorphic Geology, 28*(1), 77-96.
934 Clarke, G., Klepeis, K., & Daczko, N. (2000). Cretaceous high-P granulites at Milford Sound,
935 New Zealand: metamorphic history and emplacement in a convergent margin setting.
936 *Journal of Metamorphic Geology, 18*(4), 359-374.
937 Collier, M. L., & Kelemen, P. B. (2010). The Case for Reactive Crystallization at Mid-Ocean
938 Ridges. *Journal of Petrology, 51*(9), 1913-1940. doi:10.1093/petrology/egq043
939 Coogan, L., Saunders, A., Kempton, P., & Norry, M. (2000). Evidence from oceanic gabbros
940 for porous melt migration within a crystal mush beneath the Mid-Atlantic Ridge.
941 *Geochemistry, Geophysics, Geosystems, 1*(9).
942 Daczko, N., Clarke, G., & Klepeis, K. (2001). Transformation of two-pyroxene hornblende
943 granulite to garnet granulite involving simultaneous melting and fracturing of the lower
944 crust, Fiordland, New Zealand. *Journal of Metamorphic Geology, 19*(5), 549-562.
945 Daczko, N., Clarke, G., & Klepeis, K. (2002). Kyanite-paragonite-bearing assemblages,
946 northern Fiordland, New Zealand: rapid cooling of the lower crustal root to a
947 Cretaceous magmatic arc. *Journal of Metamorphic Geology, 20*(9), 887-902.
948 Daczko, N., Emami, S., Allibone, A., & Turnbull, I. (2012). Petrogenesis and geochemical
949 characterisation of ultramafic cumulate rocks from Hawes Head, Fiordland, New
950 Zealand. *New Zealand Journal of Geology and Geophysics, 55*(4), 361-374.
951 Daczko, N., & Halpin, J. A. (2009). Evidence for melt migration enhancing recrystallization of
952 metastable assemblages in mafic lower crust, Fiordland, New Zealand. *Journal of*
953 *Metamorphic Geology, 27*(2), 167-185.
954 Daczko, N., Klepeis, K., & Clarke, G. (2001). Evidence of Early Cretaceous collisional-style
955 orogenesis in northern Fiordland, New Zealand and its effects on the evolution of the
956 lower crust. *Journal of Structural Geology, 23*(4), 693-713.
957 Daczko, N., Piazolo, S., Meek, U., Stuart, C. A., & Elliott, V. (2016). Hornblendite delineates
958 zones of mass transfer through the lower crust. *Scientific Reports, 6*, 31369.
959 doi:10.1038/srep31369
960 De Paoli, M., Clarke, G. L., & Daczko, N. (2012). Mineral equilibria modeling of the granulite–
961 eclogite transition: effects of whole-rock composition on metamorphic facies type-
962 assemblages. *Journal of Petrology, 53*(5), 949-970.
963 Debari, S., Kay, S. M., & Kay, R. (1987). Ultramafic xenoliths from Adagdak volcano, Adak,
964 Aleutian Islands, Alaska: deformed igneous cumulates from the Moho of an island arc.
965 *The Journal of Geology, 95*(3), 329-341.
966 Diener, J. F., & Fagereng, Å. (2014). The influence of melting and melt drainage on crustal
967 rheology during orogenesis. *Journal of Geophysical Research: Solid Earth, 119*(8),
968 6193-6210.
969 Dijkstra, A. H., Barth, M. G., Drury, M. R., Mason, P. R. D., & Vissers, R. L. M. (2003).
970 Diffuse porous melt flow and melt-rock reaction in the mantle lithosphere at a slow-
971 spreading ridge: A structural petrology and LA-ICP-MS study of the Othris Peridotite
972 Massif (Greece). *Geochemistry, Geophysics, Geosystems, 4*(8), n/a-n/a.
973 doi:10.1029/2001GC000278
974 Evans, B. W., & Vance, J. A. (1987). Epidote phenocrysts in dacitic dikes, Boulder County,
975 Colorado. *Contributions to Mineralogy and Petrology, 96*(2), 178-185.

976 Fanka, A., Tsunogae, T., Daorerk, V., Tsutsumi, Y., Takamura, Y., Endo, T., & Sutthirat, C.
977 (2016). Petrochemistry and mineral chemistry of Late Permian hornblendite and
978 hornblende gabbro from the Wang Nam Khiao area, Nakhon Ratchasima, Thailand:
979 Indication of Palaeo-Tethyan subduction. *Journal of Asian Earth Sciences, 130*, 239-
980 255.
981 Fujii, N., Osamura, K., & Takahashi, E. (1986). Effect of water saturation on the distribution
982 of partial melt in the Olivine-Pyroxene-Plagioclase System. *Journal of Geophysical*
983 *Research: Solid Earth, 91*(B9), 9253-9259.
984 Fusseis, F., Regenauer-Lieb, K., Liu, J., Hough, R. M., & De Carlo, F. (2009). Creep cavitation
985 can establish a dynamic granular fluid pump in ductile shear zones. *Nature, 459*, 974.
986 doi:10.1038/nature08051
987 https://www.nature.com/articles/nature08051 - supplementary-information
988 Gardner, R. L., Piazolo, S., & Daczko, N. R. (2016). Shape of pinch and swell structures as a
989 viscosity indicator: Application to lower crustal polyphase rocks. *Journal of Structural*
990 *Geology, 88*, 32-45. doi:https://doi.org/10.1016/j.jsg.2016.04.012
991 Gardner, R. L., Piazolo, S., Evans, L., & Daczko, N. R. (2017). Patterns of strain localization
992 in heterogeneous, polycrystalline rocks – a numerical perspective. *Earth and Planetary*
993 *Science Letters, 463*, 253-265. doi:https://doi.org/10.1016/j.epsl.2017.01.039
994 Gurnis, M. (1988). Large-scale mantle convection and the aggregation and dispersal of
995 supercontinents. *332*, 695. doi:10.1038/332695a0
996 Hasalová, P, Janoušek, V., Schulmann, K., Štípská, P., & Erban, V. (2008). From orthogneiss
997 to migmatite: geochemical assessment of the melt infiltration model in the Gföhl Unit
998 (Moldanubian Zone, Bohemian Massif). *Lithos, 102*(3-4), 508-537.
999 Hasalová, P, Schulmann, K., Lexa, O., Štípská, P., Hrouda, F., Ulrich, S., . . . Týcová, P. (2008).
1000 Origin of migmatites by deformation-enhanced melt infiltration of orthogneiss: a new
1001 model based on quantitative microstructural analysis. *Journal of Metamorphic*
1002 *Geology, 26*(1), 29-53. doi:10.1111/j.1525-1314.2007.00743.x
1003 Hasalová, P, Štípská, P., Powell, R., Schulmann, K., Janoušek, V., & Lexa, O. (2008).
1004 Transforming mylonitic metagranite by open-system interactions during melt flow.
1005 *Journal of Metamorphic Geology, 26*(1), 55-80.
1006 Hollis, J. A., Clarke, G., Klepeis, K., Daczko, N., & Ireland, T. (2003). Geochronology and
1007 geochemistry of high-pressure granulites of the Arthur River Complex, Fiordland, New
1008 Zealand: Cretaceous magmatism and metamorphism on the palaeo-Pacific Margin.
1009 *Journal of Metamorphic Geology, 21*(3), 299-313.
1010 Holness, M. (2006). Melt–Solid Dihedral Angles of Common Minerals in Natural Rocks.
1011 *Journal of Petrology, 47*(4), 791-800. doi:10.1093/petrology/egi094
1012 Holness, M., Cheadle, M. J., & McKenzie, D. A. N. (2005). On the Use of Changes in Dihedral
1013 Angle to Decode Late-stage Textural Evolution in Cumulates. *Journal of Petrology,*
1014 *46*(8), 1565-1583. doi:10.1093/petrology/egi026
1015 Holness, M., Clemens, J. D., & Vernon, R. H. (2018). How deceptive are microstructures in
1016 granitic rocks? Answers from integrated physical theory, phase equilibrium, and direct
1017 observations. *Contributions to Mineralogy and Petrology, 173*(8), 62.
1018 doi:10.1007/s00410-018-1488-8
1019 Holness, M., & Sawyer, E. (2008). On the Pseudomorphing of Melt-filled Pores During the
1020 Crystallization of Migmatites. *Journal of Petrology, 49*(7), 1343-1363.
1021 doi:10.1093/petrology/egn028
1022 Jagoutz, O., Müntener, O., Schmidt, M. W., & Burg, J.-P. (2011). The roles of flux- and
1023 decompression melting and their respective fractionation lines for continental crust
1024 formation: Evidence from the Kohistan arc. *Earth and Planetary Science Letters,*
1025 *303*(1), 25-36. doi:https://doi.org/10.1016/j.epsl.2010.12.017

1026 Jamtveit, B., Putnis, C. V., & Malthe-Sørenssen, A. (2009). Reaction induced fracturing during
1027 replacement processes. *Contributions to Mineralogy and Petrology, 157*(1), 127-133.
1028 Johnston, A. D., & Wyllie, P. J. (1988). Constraints on the origin of Archean trondhjemites
1029 based on phase relationships of Nuk Gneiss with H 2 O at 15 kbar. *Contributions to*
1030 *Mineralogy and Petrology, 100*(1), 35-46.
1031 Jonas, L., Müller, T., Dohmen, R., Baumgartner, L., & Putlitz, B. (2015). Transport-controlled
1032 hydrothermal replacement of calcite by Mg-carbonates. *Geology, 43*(9), 779-782.
1033 Kelemen, P. B., Dick, H. J. B., & Quick, J. E. (1992). Formation of harzburgite by pervasive
1034 melt/rock reaction in the upper mantle. *Nature, 358*(6388), 635-641.
1035 Kelemen, P. B., Shimizu, N., & Salters, V. J. M. (1995). Extraction of mid-ocean-ridge basalt
1036 from the upwelling mantle by focused flow of melt in dunite channels. *Nature,*
1037 *375*(6534), 747-753.
1038 Klepeis, K. A., Clarke, G. L., & Rushmer, T. (2003). Magma transport and coupling between
1039 deformation and magmatism in the continental lithosphere. *GSA TODAY, 13*(1), 4-11.
1040 Korzhinskiĭ, D. S. (1959). *Physicochemical basis of the analysis of the paragenesis of minerals*:
1041 Consultants Bureau.
1042 Langone, A., Zanetti, A., Daczko, N., Piazolo, S., Tiepolo, M., & Mazzucchelli, M. (2018).
1043 Zircon U–Pb dating of a lower crustal shear zone: a case study from the northern sector
1044 of the Ivrea-Verbano Zone (Val Cannobina, Italy). *Tectonics*.
1045 Lee, A. L., Torvela, T., Lloyd, G. E., & Walker, A. M. (2018). Melt organisation and strain
1046 partitioning in the lower crust. *Journal of Structural Geology, 113*, 188-199.
1047 Lesher, C. E., & Spera, F. J. (2015). Thermodynamic and transport properties of silicate melts
1048 and magma *The Encyclopedia of Volcanoes (Second Edition)* (pp. 113-141): Elsevier.
1049 Levine, J. S. F., Mosher, S., & Rahl, J. M. (2016). The role of subgrain boundaries in partial
1050 melting. *Journal of Structural Geology, 89*, 181-196.
1051 doi:https://doi.org/10.1016/j.jsg.2016.06.006
1052 Lissenberg, C. J., MacLeod, C. J., Howard, K. A., & Godard, M. (2013). Pervasive reactive
1053 melt migration through fast-spreading lower oceanic crust (Hess Deep, equatorial
1054 Pacific Ocean). *Earth and Planetary Science Letters, 361*, 436-447.
1055 doi:https://doi.org/10.1016/j.epsl.2012.11.012
1056 Lissenberg, CJ, & Dick, H. J. (2008). Melt–rock reaction in the lower oceanic crust and its
1057 implications for the genesis of mid-ocean ridge basalt. *Earth and Planetary Science*
1058 *Letters, 271*(1-4), 311-325.
1059 Marchildon, N., & Brown, M. (2002). Grain-scale melt distribution in two contact aureole
1060 rocks: Implications for controls on melt localization and deformation. *Journal of*
1061 *Metamorphic Geology, 20*(4), 381-396.
1062 Milan, L., Daczko, N., & Clarke, G. (2017). Cordillera Zealandia: A Mesozoic arc flare-up on
1063 the palaeo-Pacific Gondwana Margin. *Scientific Reports, 7*(1), 261.
1064 Milan, L., Daczko, N., Clarke, G., & Allibone, A. (2016). Complexity of in-situ zircon U–Pb–
1065 Hf isotope systematics during arc magma genesis at the roots of a Cretaceous arc,
1066 Fiordland, New Zealand. *Lithos, 264*, 296-314.
1067 Morgan, Z., & Liang, Y. (2003). An experimental and numerical study of the kinetics of
1068 harzburgite reactive dissolution with applications to dunite dike formation. *Earth and*
1069 *Planetary Science Letters, 214*(1), 59-74. doi:https://doi.org/10.1016/S0012-
1070 821X(03)00375-3
1071 Morgan, Z., & Liang, Y. (2005). An experimental study of the kinetics of lherzolite reactive
1072 dissolution with applications to melt channel formation. *Contributions to Mineralogy*
1073 *and Petrology, 150*(4), 369-385. doi:10.1007/s00410-005-0033-8
1074 Mortimer, N., Tulloch, A., Spark, R., Walker, N., Ladley, E., Allibone, A., & Kimbrough, D.
1075 (1999). Overview of the Median Batholith, New Zealand: a new interpretation of the

1076 geology of the Median Tectonic Zone and adjacent rocks. *Journal of African earth*
1077 *sciences, 29*(1), 257-268.
1078 Naney, M. (1983). Phase equilibria of rock-forming ferromagnesian silicates in granitic
1079 systems. *American Journal of Science, 283*(10), 993-1033.
1080 Niida, K., & Green, D. H. (1999). Stability and chemical composition of pargasitic amphibole
1081 in MORB pyrolite under upper mantle conditions. *Contributions to Mineralogy and*
1082 *Petrology, 135*(1), 18-40. doi:10.1007/s004100050495
1083 Pál-Molnár, E., Batki, A., Almási, E., Kiss, B., Upton, B. G., Markl, G., . . . Harangi, S. (2015).
1084 Origin of mafic and ultramafic cumulates from the Ditrău Alkaline Massif, Romania.
1085 *Lithos, 239*, 1-18.
1086 Pandit, D., Panigrahi, M. K., & Moriyama, T. (2014). Constrains from magmatic and
1087 hydrothermal epidotes on crystallization of granitic magma and sulfide mineralization
1088 in Paleoproterozoic Malanjkhand Granitoid, Central India. *Chemie der Erde -*
1089 *Geochemistry, 74*(4), 715-733. doi:https://doi.org/10.1016/j.chemer.2014.04.008
1090 Pec, M., Holtzman, B. K., Zimmerman, M. E., & Kohlstedt, D. L. (2017). Reaction Infiltration
1091 Instabilities in Mantle Rocks: an Experimental Investigation. *Journal of Petrology,*
1092 *58*(5), 979-1003.
1093 Piazolo, S., Bestmann, M., Prior, D., & Spiers, C. (2006). Temperature dependent grain
1094 boundary migration in deformed-then-annealed material: observations from
1095 experimentally deformed synthetic rocksalt. *Tectonophysics, 427*(1-4), 55-71.
1096 Prakash, A., Piazolo, S., Saha, L., Bhattacharya, A., Pal, D. K., & Sarkar, S. (2018).
1097 Deformation behavior of migmatites: insights from microstructural analysis of a
1098 garnet–sillimanite–mullite–quartz–feldspar-bearing anatectic migmatite at Rampura–
1099 Agucha, Aravalli–Delhi Fold Belt, NW India. *International Journal of Earth Sciences*.
1100 doi:10.1007/s00531-018-1598-6
1101 Prior, D. J., Wheeler, J., Peruzzo, L., Spiess, R., & Storey, C. (2002). Some garnet
1102 microstructures: an illustration of the potential of orientation maps and misorientation
1103 analysis in microstructural studies. *Journal of Structural Geology, 24*(6), 999-1011.
1104 doi:https://doi.org/10.1016/S0191-8141(01)00087-6
1105 Putnis, A. (2009). Mineral replacement reactions. *Reviews in mineralogy and geochemistry,*
1106 *70*(1), 87-124.
1107 Rampone, Elisabetta, Borghini, G., Godard, M., Ildefonse, B., Crispini, L., & Fumagalli, P.
1108 (2016). Melt/rock reaction at oceanic peridotite/gabbro transition as revealed by trace
1109 element chemistry of olivine. *Geochimica et Cosmochimica Acta, 190*, 309-331.
1110 doi:https://doi.org/10.1016/j.gca.2016.06.029
1111 Rampone, E., Piccardo, G., Vannucci, R., Bottazzi, P., & Zanetti, A. (1994). Melt impregnation
1112 in ophiolitic peridotite: an ion microprobe study of clinopyroxene and plagioclase.
1113 *Mineralogical Magazine A, 58*, 756-757.
1114 Richet, P., Lejeune, A.-M., Holtz, F., & Roux, J. (1996). Water and the viscosity of andesite
1115 melts. *Chemical Geology, 128*(1-4), 185-197.
1116 Roselle, G. T., Baumgartner, L. P., & Chapman, J. A. (1997). Nucleation-dominated
1117 crystallization of forsterite in the Ubehebe Peak contact aureole, California. *Geology,*
1118 *25*(9), 823-826.
1119 Rosenberg, C. L., & Riller, U. (2000). Partial-melt topology in statically and dynamically
1120 recrystallized granite. *Geology, 28*(1), 7-10. doi:10.1130/0091-
1121 7613(2000)28<7:ptisad>2.0.co;2
1122 Rudnick, R. L. (1995). Making continental crust. *Nature, 378*, 571. doi:10.1038/378571a0
1123 Sanfilippo, A., Morishita, T., Kumagai, H., Nakamura, K., Okino, K., Hara, K., . . . Arai, S.
1124 (2015). Hybrid troctolites from mid-ocean ridges: inherited mantle in the lower crust.
1125 *Lithos, 232*, 124-130. doi:https://doi.org/10.1016/j.lithos.2015.06.025

1126 Sawyer, E. (1999). Criteria for the recognition of partial melting. *Physics and Chemistry of the*
1127 *Earth, Part A: Solid Earth and Geodesy, 24*(3), 269-279.
1128 Sawyer, E. (2001). Melt segregation in the continental crust: distribution and movement of
1129 melt in anatectic rocks. *Journal of Metamorphic Geology, 19*(3), 291-309.
1130 Schmidt, M. W., & Poli, S. (2004). Magmatic epidote. *Reviews in mineralogy and*
1131 *geochemistry, 56*(1), 399-430.
1132 Schröter, F., Stevenson, J., Daczko, N., Clarke, G., Pearson, N., & Klepeis, K. (2004). Trace
1133 element partitioning during high-P partial melting and melt-rock interaction; an
1134 example from northern Fiordland, New Zealand. *Journal of Metamorphic Geology,*
1135 *22*(5), 443-457.
1136 Schubert, G., Turcotte, D. L., & Olson, P. (2001). *Mantle convection in the Earth and planets*:
1137 Cambridge University Press.
1138 Schulmann, K., Martelat, J. E., Ulrich, S., Lexa, O., Štípská, P., & Becker, J. K. (2008).
1139 Evolution of microstructure and melt topology in partially molten granitic mylonite:
1140 Implications for rheology of felsic middle crust. *Journal of Geophysical Research:*
1141 *Solid Earth, 113*(B10).
1142 Scott, D. R., & Stevenson, D. J. (1986). Magma ascent by porous flow. *Journal of Geophysical*
1143 *Research: Solid Earth, 91*(B9), 9283-9296.
1144 Shaw, H. (1972). Viscosities of magmatic silicate liquids; an empirical method of prediction.
1145 *American Journal of Science, 272*(9), 870-893.
1146 Sizova, E., Gerya, T., Stüwe, K., & Brown, M. (2015). Generation of felsic crust in the
1147 Archean: a geodynamic modeling perspective. *Precambrian Research, 271*, 198-224.
1148 Sleep, N. H. (1988). Tapping of melt by veins and dikes. *Journal of Geophysical Research:*
1149 *Solid Earth, 93*(B9), 10255-10272. doi:10.1029/JB093iB09p10255
1150 Smith, D. J. (2014). Clinopyroxene precursors to amphibole sponge in arc crust. *5*, 4329.
1151 doi:10.1038/ncomms5329
1152 http://dharmasastra.live.cf.private.springer.com/articles/ncomms5329 - supplementary-
1153 information
1154 Smith, J., Piazolo, S., Daczko, N., & Evans, L. (2015). The effect of pre-tectonic reaction and
1155 annealing extent on behaviour during subsequent deformation: insights from paired
1156 shear zones in the lower crust of Fiordland, New Zealand. *Journal of Metamorphic*
1157 *Geology, 33*(6), 557-577.
1158 Solano, J. M. S., Jackson, M. D., Sparks, R. S. J., Blundy, J. D., & Annen, C. (2012). Melt
1159 Segregation in Deep Crustal Hot Zones: a Mechanism for Chemical Differentiation,
1160 Crustal Assimilation and the Formation of Evolved Magmas. *Journal of Petrology,*
1161 *53*(10), 1999-2026. doi:10.1093/petrology/egs041
1162 Spence, D. A., Sharp, P. W., & Turcotte, D. L. (1987). Buoyancy-driven crack propagation: a
1163 mechanism for magma migration. *Journal of Fluid Mechanics, 174*, 135-153.
1164 doi:10.1017/S0022112087000077
1165 Spiegelman, M., Kelemen, P. B., & Aharonov, E. (2001). Causes and consequences of flow
1166 organization during melt transport: The reaction infiltration instability in compactible
1167 media. *Journal of Geophysical Research: Solid Earth, 106*(B2), 2061-2077.
1168 Spruzeniece, L., Piazolo, S., Daczko, N., Kilburn, M., & Putnis, A. (2017). Symplectite
1169 formation in the presence of a reactive fluid: insights from hydrothermal experiments.
1170 *Journal of Metamorphic Geology, 35*(3), 281-299.
1171 Spruzeniece, L., Piazolo, S., & Maynard-Casely, H. E. (2017). Deformation-resembling
1172 microstructure created by fluid-mediated dissolution–precipitation reactions. *Nature*
1173 *communications, 8*, 14032.

1174 Stevenson, J. A., Daczko, N. R., Clarke, G. L., Pearson, N., & Klepeis, K. A. (2005). Direct
1175 observation of adakite melts generated in the lower continental crust, Fiordland, New
1176 Zealand. *Terra Nova, 17*(1), 73-79.
1177 Štípská, P., Hasalová, P., Powell, R., Závada, P., Schulmann, K., Racek, M., . . . Chopin, F.
1178 (2019). The effect of melt infiltration on metagranitic rocks: The Snieznik dome,
1179 Bohemian Massif. *Journal of Petrology*.
1180 Stowell, H., Tulloch, A., Zuluaga, C., & Koenig, A. (2010). Timing and duration of garnet
1181 granulite metamorphism in magmatic arc crust, Fiordland, New Zealand. *Chemical*
1182 *Geology, 273*(1), 91-110.
1183 Streit, J. E., & Cox, S. F. (1998). Fluid infiltration and volume change during mid-crustal
1184 mylonitization of Proterozoic granite, King Island, Tasmania. *Journal of Metamorphic*
1185 *Geology, 16*(2), 197-212. doi:10.1111/j.1525-1314.1998.00129.x
1186 Stuart, C. A., Daczko, N. R., & Piazolo, S. (2017). Local partial melting of the lower crust
1187 triggered by hydration through melt–rock interaction: an example from Fiordland, New
1188 Zealand. *Journal of Metamorphic Geology, 35*(2), 213-230.
1189 Stuart, C. A., Meek, U., Daczko, N. R., Piazolo, S., & Huang, J. X. (2018). Chemical Signatures
1190 of Melt–Rock Interaction in the Root of a Magmatic Arc. *Journal of Petrology, 59*(2),
1191 321-340. doi:10.1093/petrology/egy029
1192 Stuart, C. A., Piazolo, S., & Daczko, N. R. (2016). Mass transfer in the lower crust: Evidence
1193 for incipient melt assisted flow along grain boundaries in the deep arc granulites of
1194 Fiordland, New Zealand. *Geochemistry, Geophysics, Geosystems, 17*(9), 3733-3753.
1195 doi:10.1002/2015GC006236
1196 Stuart, C. A., Piazolo, S., & Daczko, N. R. (2018). The recognition of former melt flux through
1197 high-strain zones. *Journal of Metamorphic Geology, 36*(8), 1049-1069.
1198 doi:doi:10.1111/jmg.12427
1199 Tetley, M., & Daczko, N. (2014). Virtual Petrographic Microscope: a multi-platform education
1200 and research software tool to analyse rock thin-sections. *Australian Journal of Earth*
1201 *Sciences, 61*(4), 631-637.
1202 Turcotte, D., & Ahern, J. (1978). A porous flow model for magma migration in the
1203 asthenosphere. *Journal of Geophysical Research: Solid Earth, 83*(B2), 767-772.
1204 Vanderhaeghe, O. (1999). Pervasive melt migration from migmatites to leucogranite in the
1205 Shuswap metamorphic core complex, Canada: control of regional deformation.
1206 *Tectonophysics, 312*(1), 35-55.
1207 Vernon, R. (2011). Microstructures of melt-bearing regional metamorphic rocks. *Geological*
1208 *Society of America Memoirs, 207*, 1-11.
1209 Wade, J., Dyck, B., Palin, R. M., Moore, J. D. P., & Smye, A. J. (2017). The divergent fates of
1210 primitive hydrospheric water on Earth and Mars. *Nature, 552*, 391.
1211 doi:10.1038/nature25031
1212 Weinberg, R.F. (1996). Ascent mechanism of felsic magmas: news and views. *Geological*
1213 *Society of America Special Papers, 315*, 95-103.
1214 Weinberg, R.F. (1999). Mesoscale pervasive felsic magma migration: alternatives to dyking.
1215 *Lithos, 46*(3), 393-410.
1216 Weinberg, RF, & Searle, M. (1998). The Pangong Injection Complex, Indian Karakoram: a
1217 case of pervasive granite flowthrough hot viscous crust. *Journal of the Geological*
1218 *Society, 155*(5), 883-891.
1219 Wu, K., Ling, M. X., Hu, Y. B., Guo, J., Jiang, X. Y., Sun, S. J., . . . Sun, W. (2018).
1220 Melt-Fluxed Melting of the Heterogeneously Mixed Lower Arc Crust: A Case Study
1221 from the Qinling Orogenic Belt, Central China. *Geochemistry, Geophysics,*
1222 *Geosystems, 19*(6), 1767-1788.

Závada, P., Schulmann, K., Konopásek, J., Ulrich, S., & Lexa, O. (2007). Extreme ductility of feldspar aggregates—Melt-enhanced grain boundary sliding and creep failure: Rheological implications for felsic lower crust. *Journal of Geophysical Research: Solid Earth, 112*(B10).

Závada, P., Schulmann, K., Racek, M., Hasalová, P., Jeřábek, P., Weinberg, R. F., . . . Roberts, A. (2018). Role of strain localization and melt flow on exhumation of deeply subducted continental crust. *Lithosphere, 10*(2), 217-238.

Zen, E.-A., & Hammarstrom, J. M. (1984). Magmatic epidote and its petrologic significance. *Geology, 12*(9), 515-518.

FIGURE CAPTIONS

Figure 1. Field relationships of the hornblende-rich bodies studied, Pembroke Valley, Fiordland, New Zealand. a) Aerial view of the site 1 hornblende-rich body (H, white dashed lines) hosted within two-pyroxene-pargasite gneiss. Structural map 1b marked by white rectangle. Inset: locality of field area (red star) within northern part of the Fiordland Magmatic Provenance (black). b) Structural field map of the site 1 hornblende-rich body, showing hornblende-rich body (H), surrounded by a hydration halo termed Transition Zone (TZ) within two-pyroxene-pargasite, gabbroic gneiss (GG) c),d), Field photographs of site 2 hornblende-rich body, surrounded by TZ, located a few hundred metres lower in the valley. This body is much thinner than the site 1 hornblende-rich body; note camera cap (diameter 5 cm) for scale.

Figure 2: Field relationships and microstructures of the two pyroxene-pargasite-gneiss, gabbroic gneiss (GG) which forms the host and precursor rock. a) Outcrop photograph of the host with S_1 gneissosity, featuring rectilinear garnet reaction zones (GRZ). Inset shows gneissosity is unaffected by GRZ i.e. it is continuous from host into GRZ. b) Photomicrograph showing mafic clusters of enstatite, diopside and pargasite defining the S_1 gneissosity, hosted within a predominantly plagioclase-rich matrix, plane polarised light, c) Photomicrograph of a garnet reaction zone (GRZ), showing partial replacement of diopside and enstatite by garnet, plane polarised light.

Figure 3: Field characteristics of the hornblende-rich body. a) Clinozoisite-hornblendite (>10% cz, H(Cz-Hbl)) and hornblendite (H(Hbl)) (<10% cz)), contact highlighted by dashed

white line. Garnetite stringers are present in both rock units (double white arrows). b) Pegmatite bodies within, and enclosing, both H(Hbl) and H(Cz-Hbl) (inset). Pegmatite consists of coarse-grained hornblende (yellow arrows), garnet (white arrows) and plagioclase (red arrows). Garnetite stringers found throughout. The boundaries of the pegmatite are diffuse. c) Close-up of garnetite stringer predominantly consisting of garnet (H(Grt)) within hornblende-rich body, large 1 cm wide garnet porphryoblasts (white arrow) are present. d) Garnet porphryoblasts within the transition zone (white arrows), close to the boundary of the two units (separated by white dashed lines). Inset shows several garnet euhedral porphryoblasts which are surrounded by thin felsic rims; a common feature within the TZ; garnet is up to 10 cm wide.

Figure 4: Field characteristics of the transition zone and hornblende-rich body relationship. a) Modified garnet reaction zones (GRZ) in transition zone. Garnet surrounded by either plagioclase or hornblende (white arrows) or both (red arrows). Contact boundary highlighted by white dashed line. b) Highly irregular contact boundary between hornblende-rich body (H) and TZ. In this area, H protrudes out in a finger-like pattern, often linked to modified GRZ in the TZ. c) Another hornblende-rich body in the valley with protrusions at the TZ-H boundary. d) Regular contact boundary between H and TZ (white line) as is the contact between TZ and GG (black line). e) Large lozenge-shaped TZ “remnants” within the H body (also refer to Fig. 1b). f) Small rounded TZ “remnant” within H (near H-TZ boundary) where garnetite stringers appear to deflect around (double white arrows). Porphyroblastic garnet abundant here (white arrows).

Figure 5: Field characteristics of the GRZ and their relationship to different main lithologies. a) Field map of close-up relationships of the northern side of the hornblende-rich body (area marked in Fig. 1b). Modified GRZ (grey) within the transition zone swing in and become sub-parallel to the hornblende-rich body, as a result of sinistral shearing. Several of these

1278 modified GRZ can be traced directly into the hornblende-rich body where they are
1279 transformed to garnetite stringers (white), and are intensely deformed, dismembered and
1280 folded. Porphyroblastic garnets found throughout the TZ. b) Field map of the southern side of
1281 the hornblende-rich body (area marked in Fig. 1b; note: GRZ within the two-pyroxene-
1282 pargasite gneiss in three orientations (light grey). GRZ perpendicular to the hornblende-rich
1283 body are bent due to strain from sinistral shearing. They are complexly deformed within the
1284 TZ (grey) and some lead directly into the hornblende-rich body (white). Porphyroblastic
1285 garnets found throughout the TZ. c) Close-up of modified GRZ within the TZ; these are
1286 typically surrounded by either hornblende (upper) or plagioclase (lower). d) Modified GRZ;
1287 note that a single GRZ may be surrounded by hornblende (hbl) and then plagioclase (pl)
1288 along strike. e) Modified GRZ seen within the hornblende-rich body where they are now
1289 garnetite stringers. In this image, garnetite stringers preserve orientation relationships closely
1290 resembling those seen in the host rock; i.e. they are rectilinear. f), g), h) Garnetite stringers
1291 are variably deformed, where they show apparent “M” folds (f), “S” and “Z” open to tight
1292 folds (g), to sheath folds (h).

1293 Figure 6: Whole rock geochemistry of gabbroic gneiss (1 sample) transition zone (1 sample),
1294 clinozoisite-hornblendite (3 samples) and hornblendite (3 samples). Harker style diagram with
1295 SiO_2 content on the x-axis and weight percent oxide (wt. %) for Fe_2O_3, Na_2O and MgO on the
1296 y-axis. LOI values presented by white box per sample with values corresponding to right-hand
1297 side.

1298 Figure 7: Microstructural characteristics of clinozoisite-hornblendite rock and garnetite
1299 stringer a) Photomicrograph in plane polarised light of clinozoisite-hornblendite H(Cz-Hbl)
1300 and a garnetite stringer H(Grt). Scale bar is 1mm. BSE and EBSD areas are marked and
1301 boundary between the two is outlined by a dashed line. b) BSE of H(Cz-Hbl) area showing
1302 interstitial plagioclase (pl) films along grain boundaries of both clinozoisite (cz) and

hornblende (hbl). White arrows indicate dihedral angles as low as <10°. Inset shows crystallographic orientation map for pl, (cz and hbl phase colours), note plagioclase is not connected in 2D but has the same crystallographic orientation, hence must be connected in 3D. Area for c) marked. c) Inclusions within cz grain are often hbl (see a)). However, in this area they are multiphase crystallisations. d) EBSD based phase map of clinozoisite-hosted multiphase inclusion mineral phases (cz, pl, hbl, clinochlore, K-feldspar), scale bar 50 μm. e) crystallographic orientation map of clinozoisite-hosted multiphase inclusions. Cz host and cz within inclusions have same orientation. Pl twin set (noted) and hbl each have their own orientation that is the same (i.e. there is one main pl twin set, hbl has the same orientation throughout). Clinochlore exhibits the same orientation where found. Sale bar 50 μm. f) & g) Example BSE images of low dihedral angles of pl, where white arrows indicate angles as low as 10°. Scale bars 100 μm. h) BSE image of contact with garnetite stringer. Note irregularly shaped plagioclase grain with some very low dihedral angles of plagioclase and hornblende (white arrows). Hosted within the plagioclase is rutile (rt) and apatite (ap). i) Crystallographic orientation map for plagioclase, note plagioclase is a single grain with a consistent twin set orientation (see pole figure, twin shown by colours).

Figure 8: Microstructural characteristics of hornblendite and garnetite stringer. a) Photomicrograph plane polarised light of hornblendite H(Hbl) and a garnetite stringer H(Grt). Scale bar is 1mm. BSE and EBSD areas are marked. b) BSE of multiphase crystallisations found within hornblendite. Note very low dihedral angles at several ends, <10° (white arrows). Phases found are plagioclase (pl), biotite (bt), garnet (grt) and rutile (rt). Note that plagioclase is irregularly shaped. Bt have nice crystal faceting and garnet has corroded crystal shapes. c) EBSD-based phase map. d) Same area as shown in (c), crystallographic orientations for plagioclase and garnet shown as varying colours; hornblende is shown as a

1327 phase in green. Note there are two main plagioclase twin sets that are found (marked). Garnet
1328 orientation colouring and pole figure shows garnet grains have the same orientation.

1329 Figure 9: Microstructural characteristics of garnetite stringers within hornblende-rich body. a)
1330 BSE image of garnetite stringer showing garnet (grt), hornblende (hbl) grains and interstitial
1331 plagioclase (pl), and minor ilmenite (ilm). White arrows point to very low dihedral angles of
1332 plagioclase and hornblende (<10°). Box outlines area of b-d. b) Garnet (red) and hornblende
1333 (green) with interstitial plagioclase. Plagioclase crystallographic orientation colouring shows
1334 two interconnected grain networks (black arrows, 1 & 2) where plagioclase grains not
1335 connected in 2D show the same orientation, hence must be connected in 3D. c) Garnet (red)
1336 and plagioclase (blue) as phase colours. Crystallographic orientations of hornblende show three
1337 separate grains which each exhibit anhedral hornblende crystal shapes. d) Hornblende and
1338 plagioclase, from above, in white. Garnet crystallographic orientation colouring shows a mix
1339 of rounded garnets, to amoeboidal grain shapes and sub-grains. Severe lattice distortion
1340 showing no systematic preference of orientation are highlighted with low degree boundaries.
1341 A <111> pole figure of blue strongly distorted grain shows an irregular orientation spread,
1342 within slightly distorted intracrystal misorientations. Comparatively, crystallographic
1343 orientations of all garnet grains (as one point per grain) showing there is a lack of preferred
1344 orientation across garnetite stringers; note that the same colour scheme is used in the pole
1345 figures and (d). e) Hornblende and plagioclase (from 7h) in phase colours. Crystallographic
1346 orientation colouring shown for garnet only. Note lattice distortions within individual grains.

1347 Figure 10: Microstructural characteristics of hornblendite (Hbl) – transition zone (TZ)
1348 boundary. a) Photomicrograph showing boundary, plane polarised light; note S_1 gneissosity;
1349 scale bar is 1 cm and SEM and EBSD areas are marked as black boxes. b) Plagioclase
1350 orientation map shows two main plagioclase grains within the transition zone. Two main twin
1351 sets reveal deformation twinning with tapered twins. Small plagioclase grains show no

1352 deformation twinning or other deformation features (inset). Remnant islands of plagioclase
1353 grains found enclosed within hornblende are shown with black arrows; c) Hornblende
1354 orientation colour map (inset, BSE image of EBSD area with shape marked). Note various
1355 crystallographic orientations of hornblende grains, independent of the plagioclase grain it
1356 surrounds. Hornblende is found surrounding plagioclase and at triple junctions (top, smaller
1357 grains) and at a plagioclase twin boundary. Similar to b) small grains showing random
1358 orientations occur at pl-hbl boundaries. d) BSE image near contact boundary, marked in a)
1359 showing enclosure of plagioclase grain in hornblende grain. e) Hornblende in white and
1360 plagioclase crystallographic orientations shown. Note a remnant sub-grain of plagioclase,
1361 surrounded by hornblende (black arrow). Hornblende has irregular cuspate-lobate boundaries,
1362 atypical of hornblende crystal shapes.

1363 Figure 11: Evolution of the microstructure with increasing melt flux leading to the identified
1364 microstructural characteristics. Stage 1: Externally-derived melt infiltrates the pre-existing
1365 gabbroic gneiss via porous melt flow (likely deformation-assisted), where melt moves along
1366 grain boundaries; Stage 2: at the immediate contact boundary between the transition zone and
1367 hornblende-rich body; (i) remnant islands of old plagioclase sub-grains, (ii) local precipitation
1368 of new, fine-grained plagioclase of evolving composition, (iii) some equilibrated hornblende-
1369 plagioclase boundaries, (iv) pointed melt films at melt front, and (v) highly irregular
1370 hornblende-plagioclase grain boundaries along reaction front. Stage 3: During increased melt
1371 flux and melt-rock reactions, microstructures evolve from μm-mm scale instabilities to
1372 subhedral to anhedral, igneous-like crystal faces of hornblende and clinozoisite. Clinozoisite
1373 with hornblende inclusions, due to coeval crystallisation, and garnetite. Microstructures
1374 indicative of the former presence of melt include (vi) plagioclase melt films along grain
1375 boundaries, some with low dihedral angles as low as <10º (where growth twin crystallographic
1376 orientations indicate interconnected 3D melt networks), (vii) plagioclase and hornblende films

within garnetite, with some low dihedral angles, (viii) melt pocket crystallisations and (ix) severe crystallographic lattice distortions.

TABLE CAPTIONS

Table 1. Characteristics of the main rock types of this study.

SUPPORTING INFORMATION

Additional Supporting Information may be found in the online version of this article at the publisher's web site:

Figure S1. Histogram of measured apparent low dihedral angles (200 measurements). Note that some apparent low dihedral angles are as low as <10° and that there is a relatively even spread of apparent low dihedral angles between those <10° and those <60°. BSE images from which the apparent low dihedral angles were measured are shown as examples. White arrows point to the examples of measured angles.

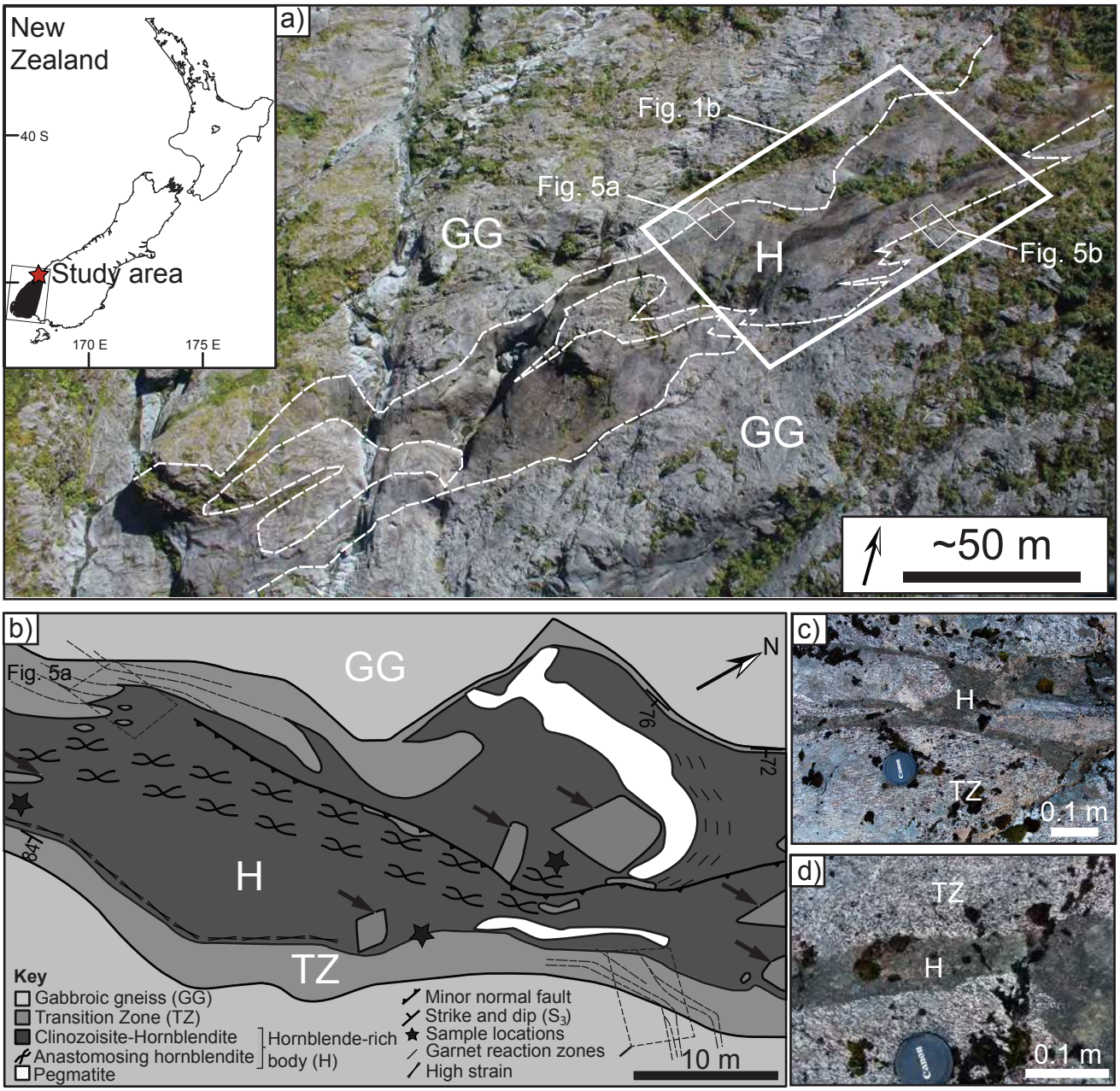
a)
New Zealand
40 S
Study area
170 E
175 E
Fig. 1b
Fig. 5a
Fig. 5b
GG
H
GG
~50 m
b)
Fig. 5a
GG
N
H
TZ
Key
Gabbroic gneiss (GG)
Transition Zone (TZ)
Clinozoisite-Hornblendite
Anastomosing hornblendite
Pegmatite
Hornblende-rich body (H)
Minor normal fault
Strike and dip (S3)
Sample locations
Garnet reaction zones
High strain
10 m
c)
H
TZ
0.1 m
d)
TZ
H
0.1 m

Figure 1

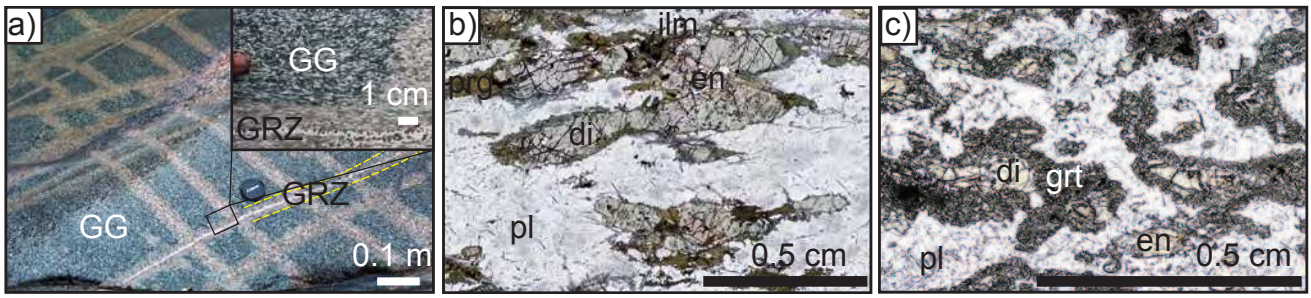

Figure 2

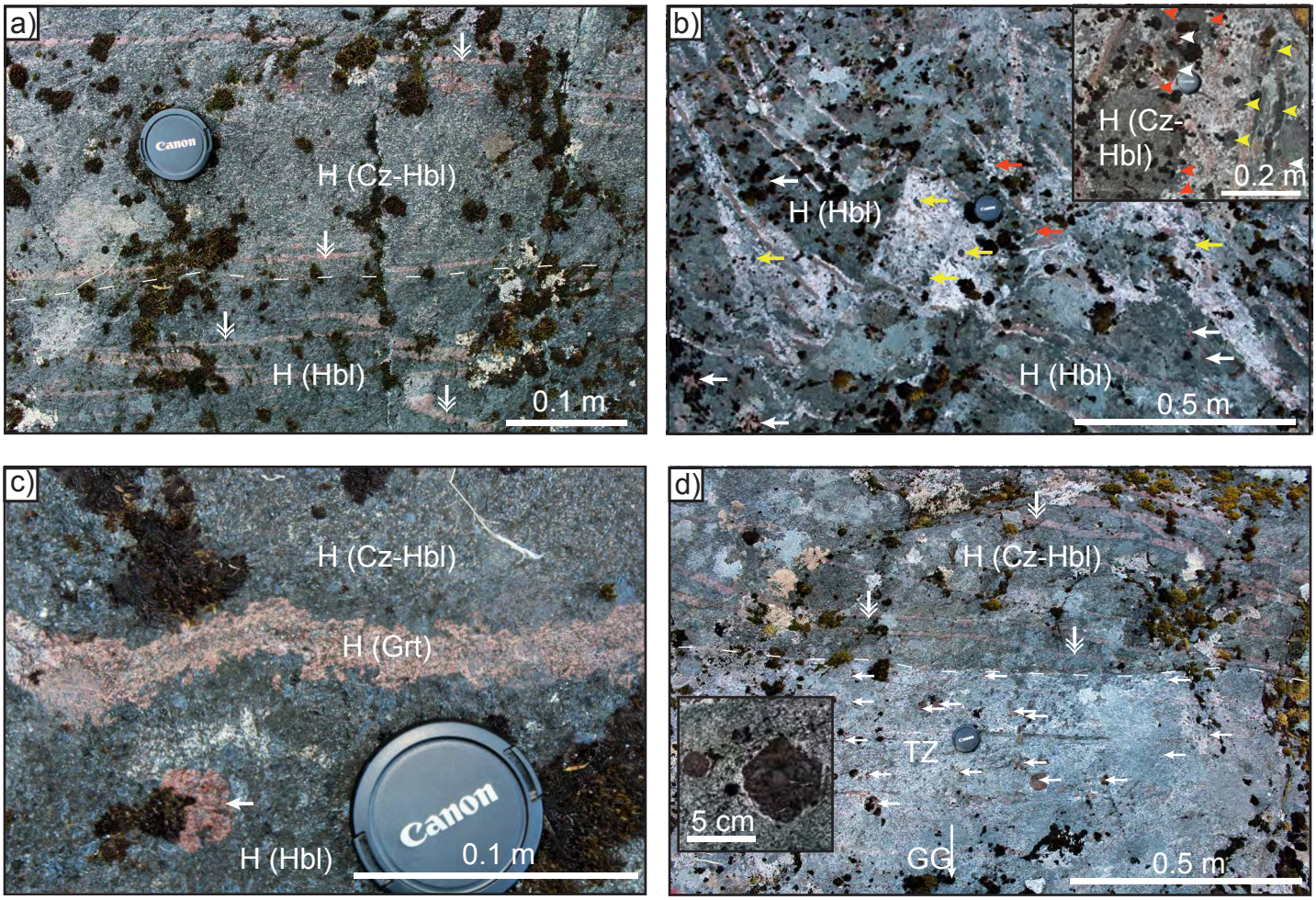
a)
H (Cz-Hbl)
H (Hbl)
0.1 m
b)
H (Cz-Hbl)
0.2 m
H (Hbl)
H (Hbl)
0.5 m
c)
H (Cz-Hbl)
H (Grt)
H (Hbl)
0.1 m
d)
H (Cz-Hbl)
TZ
5 cm
GC
0.5 m

Figure 3

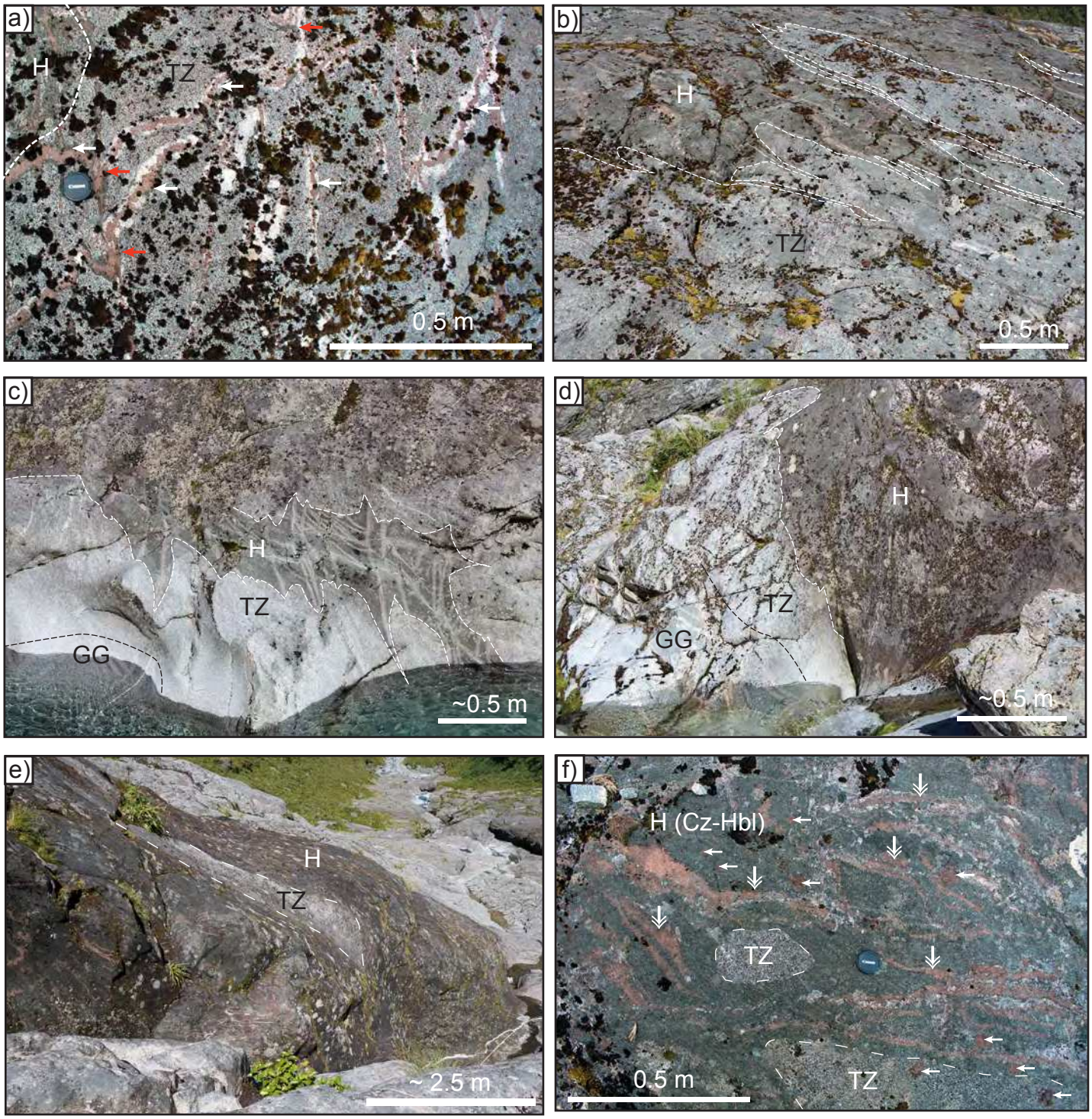
a)
H
TZ
0.5 m
b)
H
TZ
0.5 m
c)
H
TZ
GG
~0.5 m
d)
H
TZ
GG
~0.5 m
e)
H
TZ
~ 2.5 m
f)
H (Cz-Hbl)
TZ
0.5 m
TZ

Figure 4

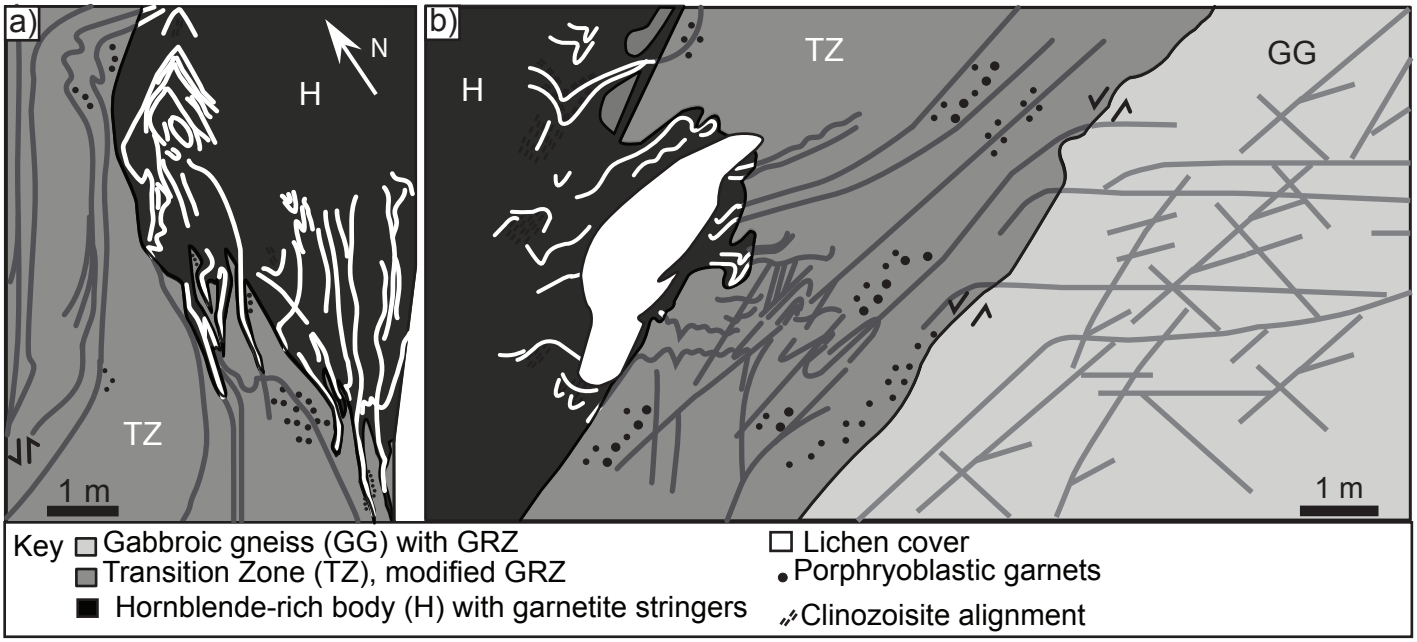
a)
N
H
TZ
1 m
b)
H
TZ
GG
1 m
Key
Gabbroic gneiss (GG) with GRZ
Transition Zone (TZ), modified GRZ
Hornblende-rich body (H) with garnetite stringers
Lichen cover
Porphryoblastic garnets
Clinozoisite alignment

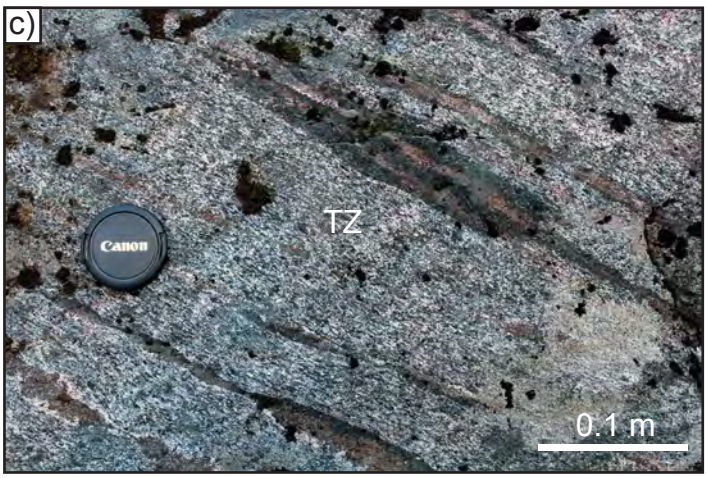
c)
TZ
0.1 m

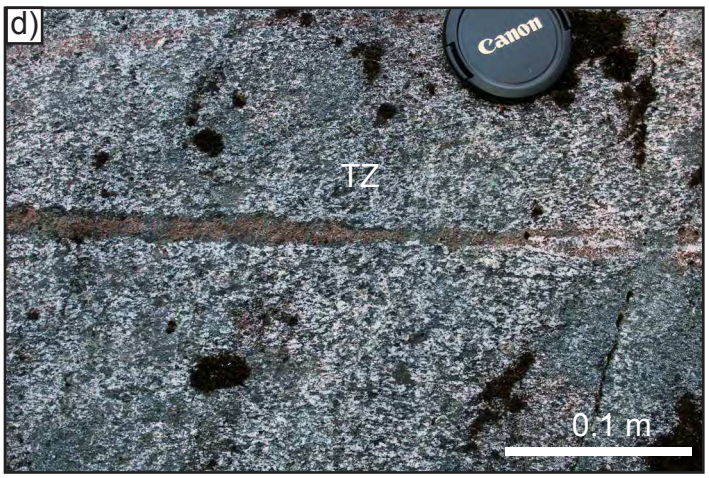
d)
TZ
0.1 m

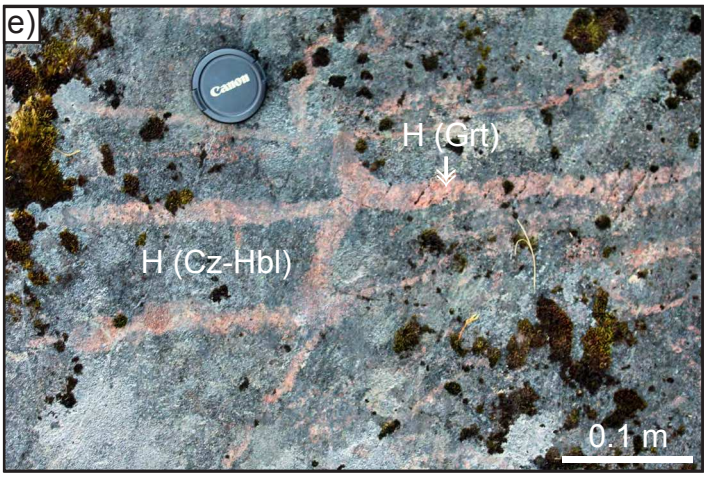
e)
H (Grt)
H (Cz-Hbl)
0.1 m

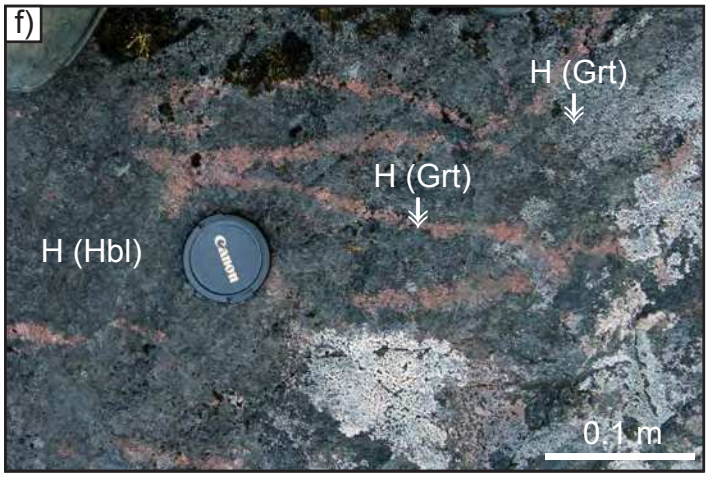
f)
H (Grt)
H (Grt)
H (Hbl)
0.1 m

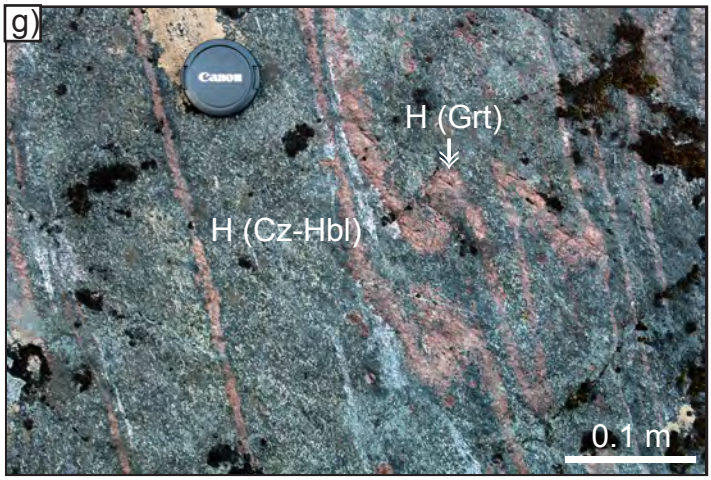
g)
H (Grt)
H (Cz-Hbl)
0.1 m

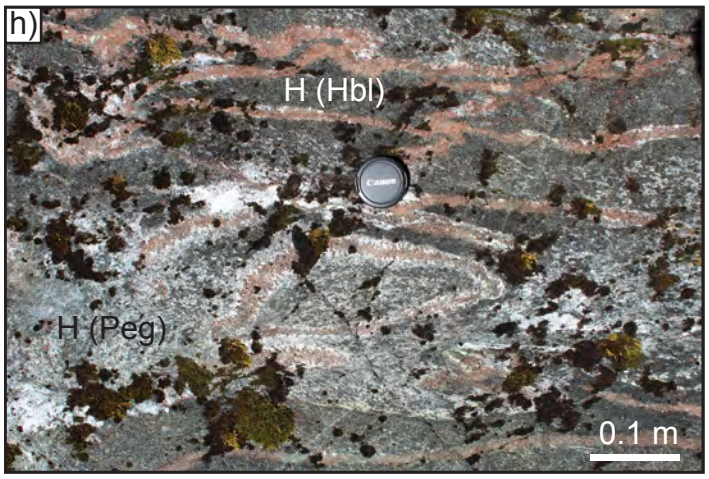
h)
H (Hbl)
H (Peg)
0.1 m

Figure 5

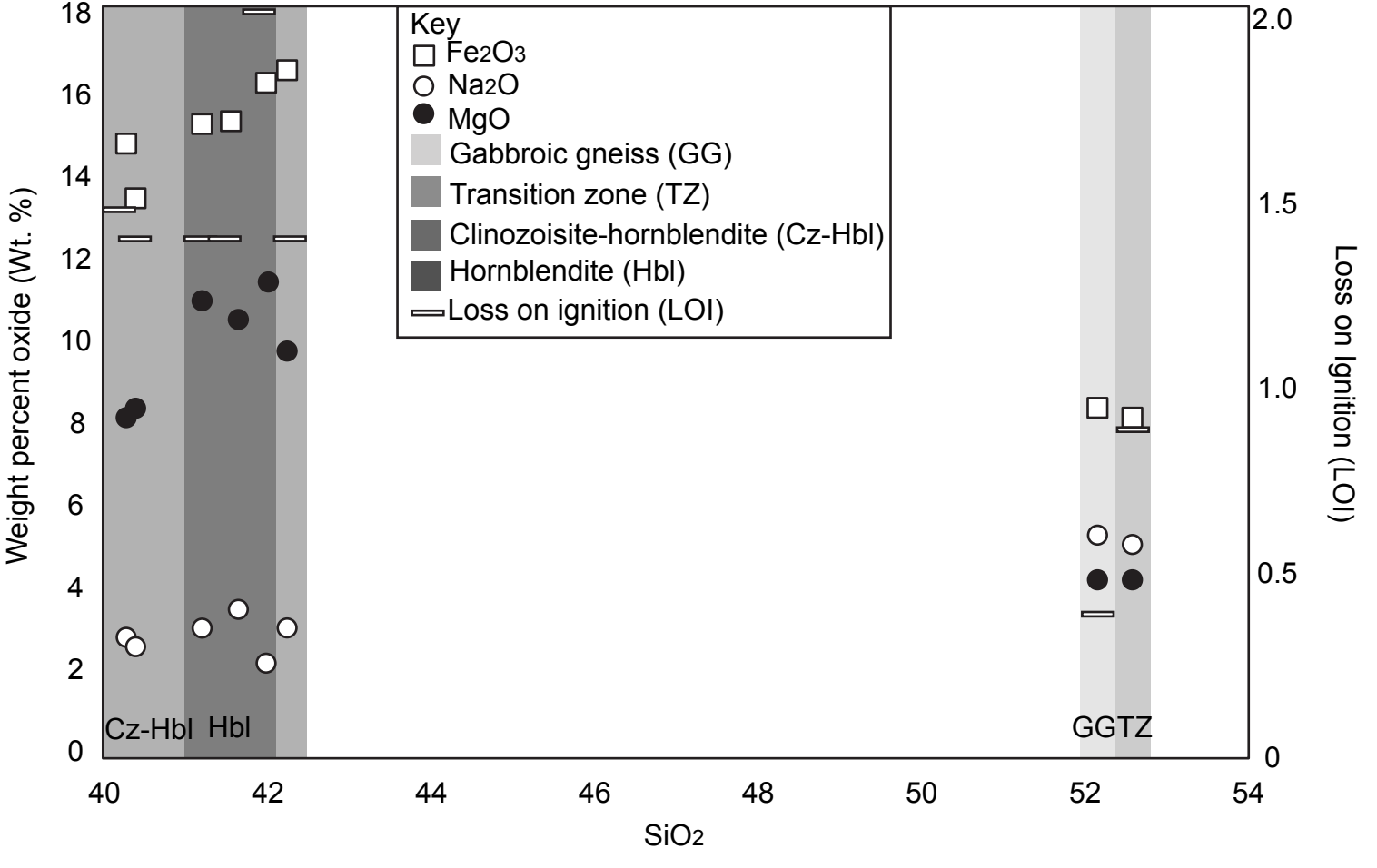
Key
Fe2O3
Na2O
MgO
Gabbroic gneiss (GG)
Transition zone (TZ)
Clinozoisite-hornblendite (Cz-Hbl)
Hornblendite (Hbl)
Loss on ignition (LOI)
Weight percent oxide (Wt. %)
Loss on Ignition (LOI)
SiO2
Cz-Hbl
Hbl
GG
TZ
0
2
4
6
8
10
12
14
16
18
0
0.5
1.0
1.5
2.0
40
42
44
46
48
50
52
54

Figure 6

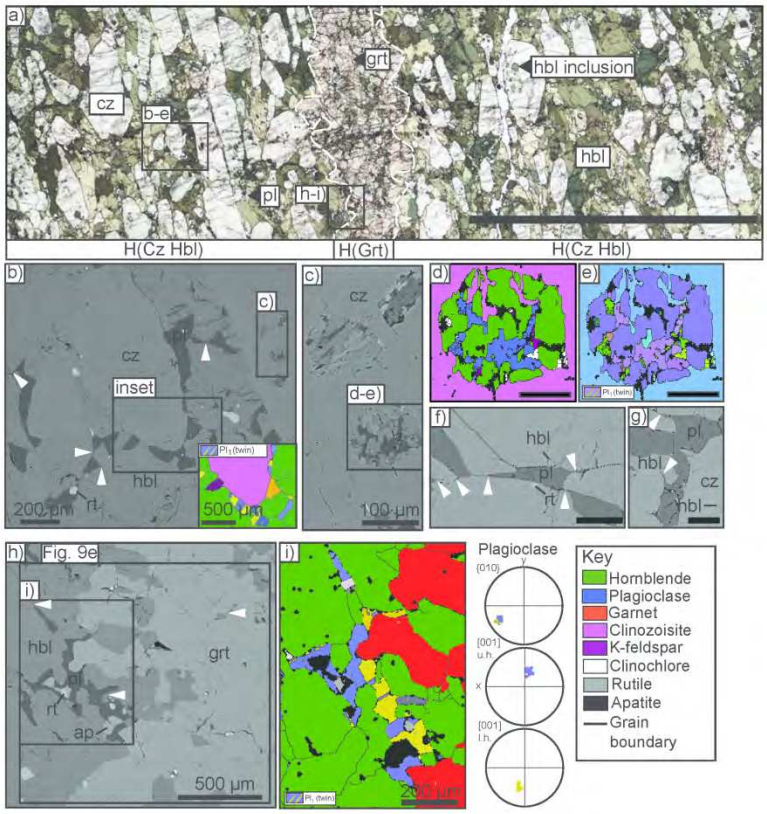

Figure 7

215x279mm (300 x 300 DPI)

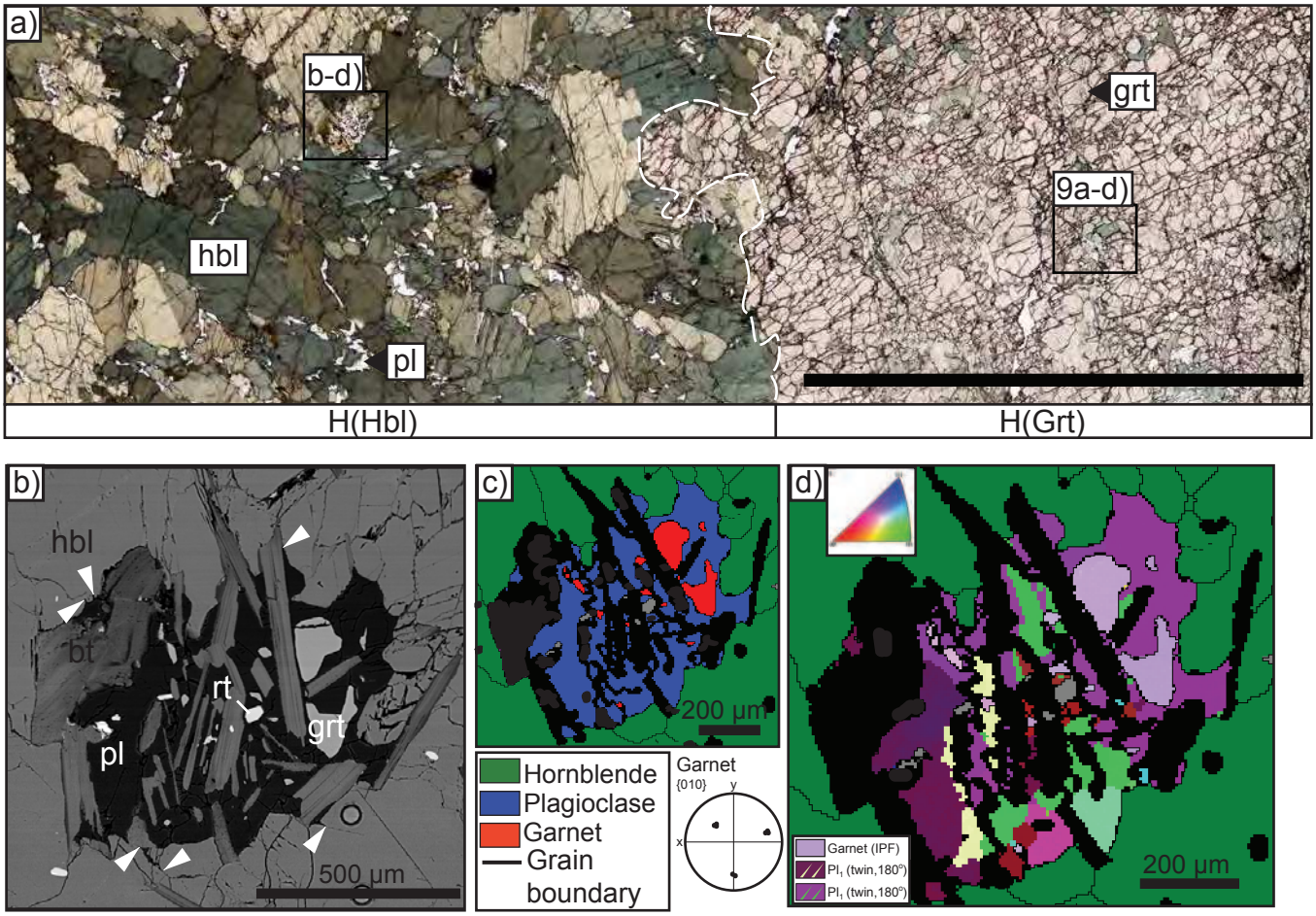
a)
b-d)
grt
9a-d)
hbl
pl
H(Hbl)
H(Grt)
b)
hbl
bt
rt
grt
pl
500 µm
c)
200 µm
Hornblende
Plagioclase
Garnet
Grain boundary
Garnet {010}
y
x
d)
Garnet (IPF)
Pl1 (twin,180°)
Pl1 (twin,180°)
200 µm

Figure 8

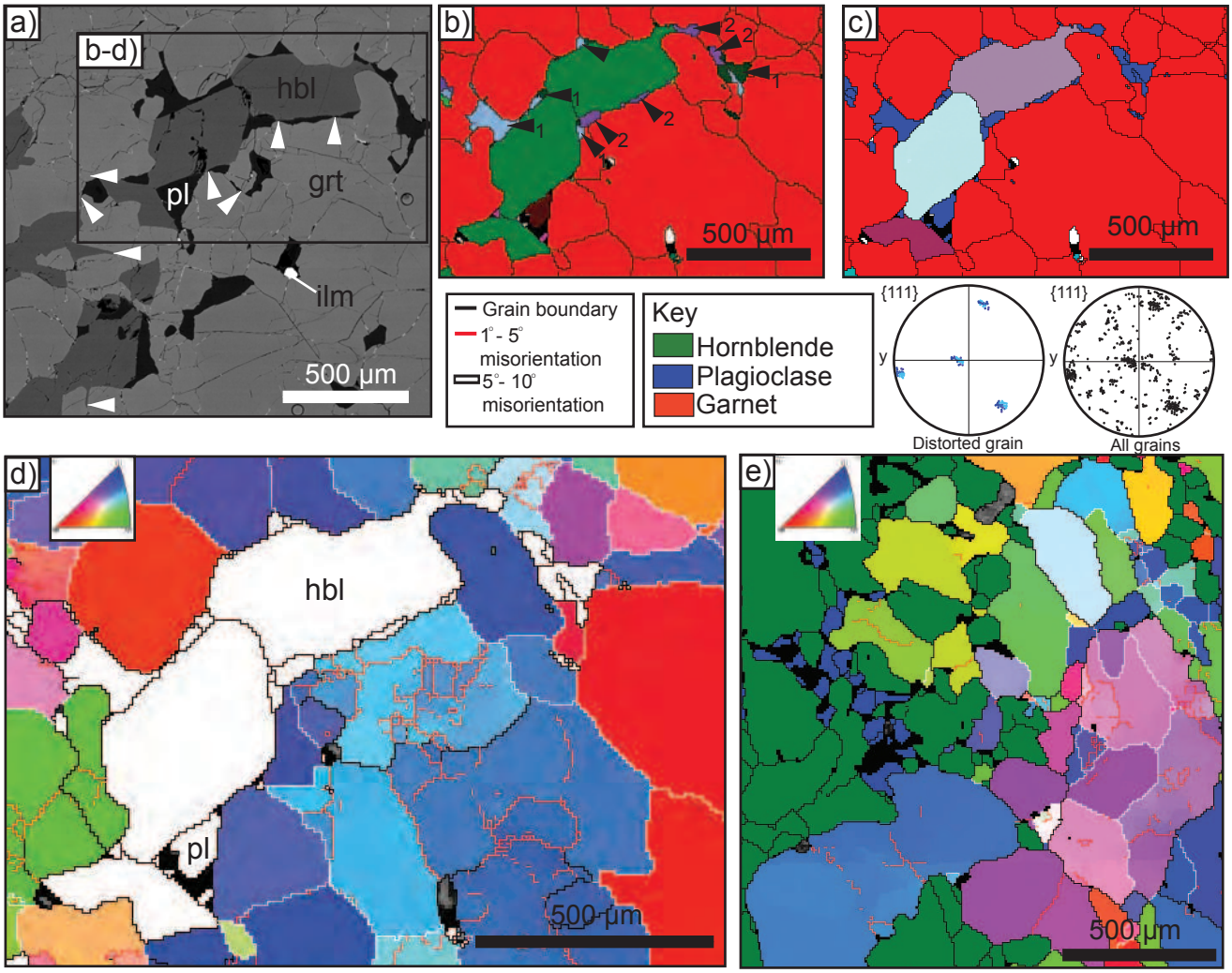
a)
b-d)
hbl
pl
grt
ilm
500 µm
b)
500 µm
c)
500 µm
Grain boundary
1° - 5° misorientation
5° - 10° misorientation
Key
Hornblende
Plagioclase
Garnet
{111}
y
Distorted grain
{111}
y
All grains
d)
hbl
pl
500 µm
e)
500 µm

Figure 9

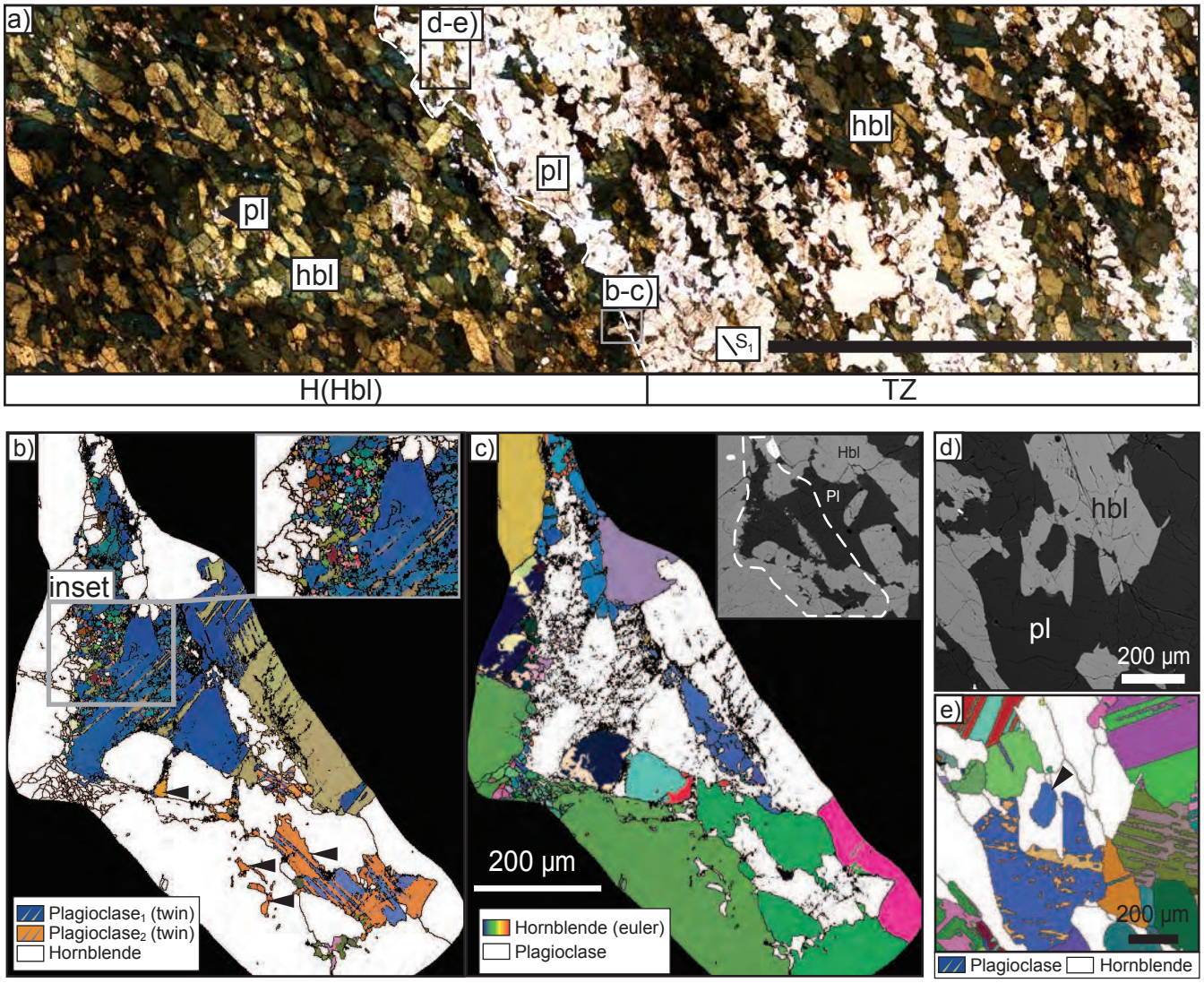
a)
d-e)
hbl
pl
pl
hbl
b-c)
S1
H(Hbl)
TZ
b)
inset
Plagioclase1 (twin)
Plagioclase2 (twin)
Hornblende
c)
Hbl
Pl
200 µm
Hornblende (euler)
Plagioclase
d)
hbl
pl
200 µm
e)
200 µm
Plagioclase
Hornblende

Figure 10

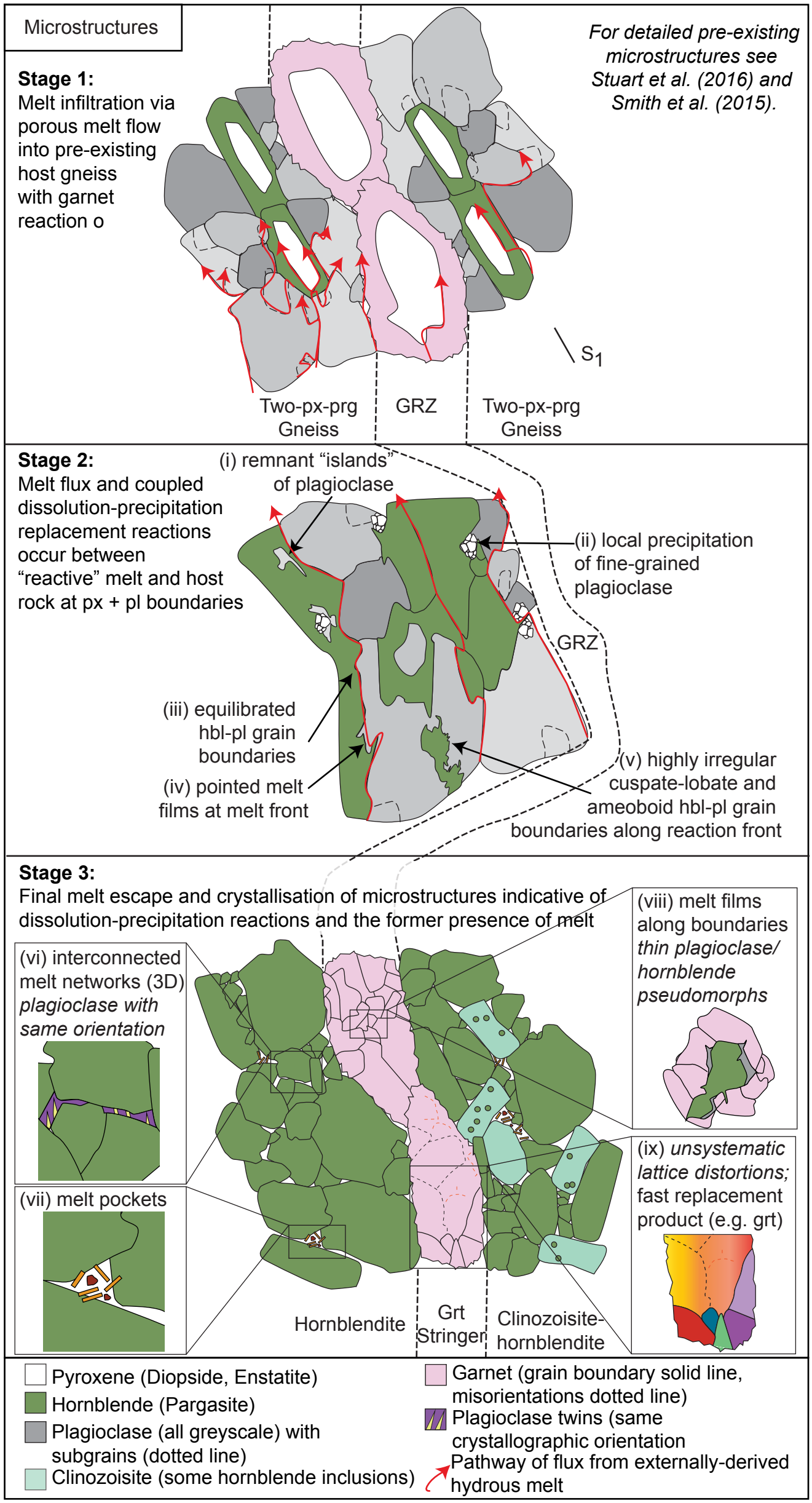
Microstructures
Stage 1:
Melt infiltration via porous melt flow into pre-existing host gneiss with garnet reaction o
For detailed pre-existing microstructures see Stuart et al. (2016) and Smith et al. (2015).
S1
Two-px-prg Gneiss
GRZ
Two-px-prg Gneiss
Stage 2:
Melt flux and coupled dissolution-precipitation replacement reactions occur between "reactive" melt and host rock at px + pl boundaries
(i) remnant "islands" of plagioclase
(ii) local precipitation of fine-grained plagioclase
GRZ
(iii) equilibrated hbl-pl grain boundaries
(iv) pointed melt films at melt front
(v) highly irregular cuspate-lobate and ameoboid hbl-pl grain boundaries along reaction front
Stage 3:
Final melt escape and crystallisation of microstructures indicative of dissolution-precipitation reactions and the former presence of melt
(vi) interconnected melt networks (3D) plagioclase with same orientation
(vii) melt pockets
(viii) melt films along boundaries thin plagioclase/ hornblende pseudomorphs
(ix) unsystematic lattice distortions; fast replacement product (e.g. grt)
Hornblendite
Grt Stringer
Clinozoisite-hornblendite
Pyroxene (Diopside, Enstatite)
Hornblende (Pargasite)
Plagioclase (all greyscale) with subgrains (dotted line)
Clinozoisite (some hornblende inclusions)
Garnet (grain boundary solid line, misorientations dotted line)
Plagioclase twins (same crystallographic orientation
Pathway of flux from externally-derived hydrous melt

Figure 11

Table 1. Characteristics of the main rock types of this study.

Rock unit	**Rock type**	**Mineralogy (area %)**	**Ductile features**	**Presence of GRZ (original bold, modified italic)**	**Microstructures indicative of the former presence of melt**
Gabbroic Gneiss (GG)	*Two pyroxene-pargasite gneiss*	~45 pl 20 hbl (± minor qtz sym) ~15 cpx ~10 opx Minor cz, ky, ap, ru, ilm	Yes - S_1 magmatic foliation	**GRZ**	No
Hornblende-rich body (H)	*Clinozoisite-hornblendite (H(Cz-Hbl)*	10–50 cz 50–95 hbl Minor pl, grt	No	*GRZ*	Yes - pl films - 3D networks - melt pocket
	Hornblendite (H(Hbl))	95 hbl Minor pl, grt	No	*GRZ*	Yes - pl films - 3D networks - melt pocket
	Garnetite	90–95 grt Minor hbl, pl	No	*GRZ*	Yes - pl/hbl films - 3D networks - grt lattice distortion
Transition Zone (TZ)	*Hornblende-feldspar gneiss*	~45 pl 45 hbl (± minor qtz sym) Minor cz, ky, ap, ru, ilm	Yes - S_1 magmatic foliation - S_3 shear zone foliation	*GRZ*	Yes - large grt with surrounding leucosome -unreacted remnant bodies

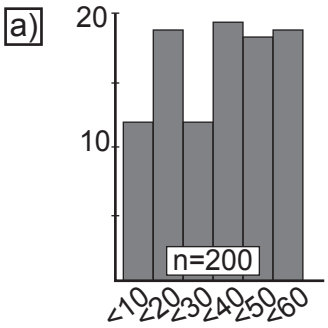
a)
20
10
n=200
<10
20
30
40
50
60

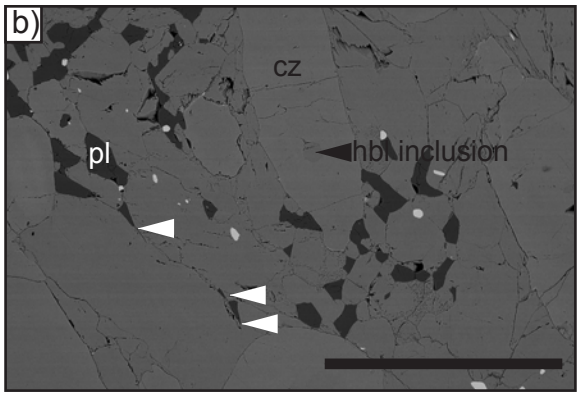
b)
cz
pl
hbl inclusion

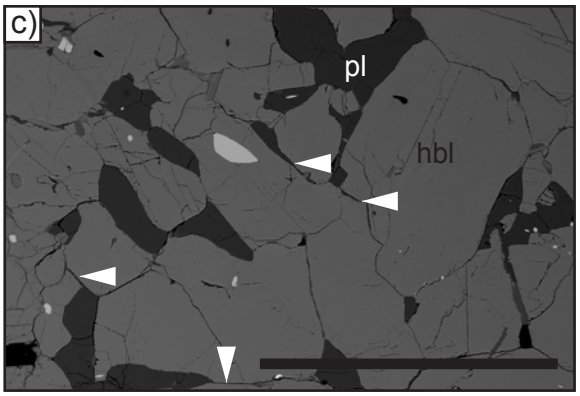
c)
pl
hbl

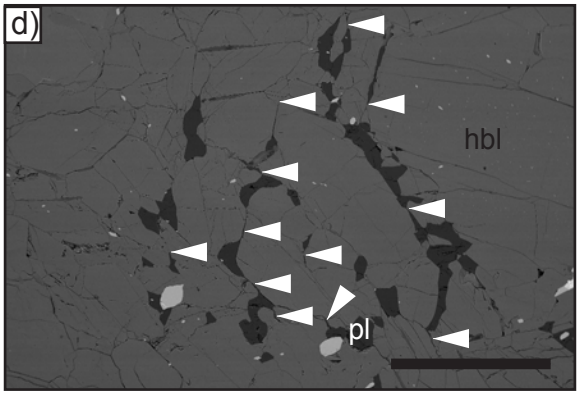
d)
hbl
pl

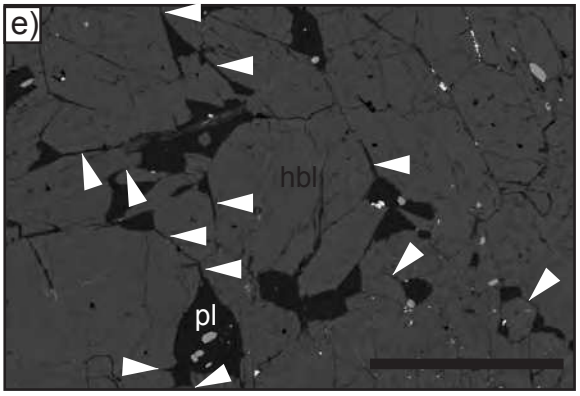
e)
hbl
pl